Damaged mitochondria recruit the effector NEMO to activate NF-κB signaling

Olivia Harding[1,2], **Elisabeth Holzer**[2,3,4,5], **Julia F. Riley**[1,2], **Sascha Martens**[2,3,4], **Erika L.F. Holzbaur**[1,2,*]

[1]Department of Physiology, Perelman School of Medicine, University of Pennsylvania, Philadelphia, PA, 19104

[2]Aligning Science Across Parkinson's (ASAP) Collaborative Research Network, Chevy Chase, MD, 20815

[3]Max Perutz Labs, Vienna Biocenter Campus, Vienna, Austria

[4]Center for Molecular Biology, Department of Biochemistry and Cell Biology, University of Vienna, Vienna

[5]Austria; Vienna Biocenter PhD Program, a Doctoral School of the University of Vienna and Medical University of Vienna, Vienna, Austria.

Summary

Failure to clear damaged mitochondria via mitophagy disrupts physiological function and may initiate damage signaling via inflammatory cascades, though how these pathways intersect remains unclear. We discovered that NF-κB essential regulator NEMO is recruited to damaged mitochondria in a Parkin-dependent manner in a time-course similar to recruitment of the structurally-related mitophagy adaptor, OPTN. Upon recruitment, NEMO partitions into phase-separated condensates distinct from OPTN, but colocalizing with p62/SQSTM1. NEMO recruitment in turn recruits the active catalytic IKK component phospho-IKKβ, initiating NF-κB signaling and the upregulation of inflammatory cytokines. Consistent with a potential neuroinflammatory role, NEMO is recruited to mitochondria in primary astrocytes upon oxidative stress. These findings suggest that damaged, ubiquitinated mitochondria serve as an intracellular platform to initiate innate immune signaling, promoting the formation of activated IKK complexes sufficient to activate NF-kB signaling. We propose that mitophagy and NF-κB signaling are initiated as parallel pathways in response to mitochondrial stress.

eTOC blurb

Mitochondrial dysfunction and neuroinflammation are implicated in neurodegeneration, prompting investigations into how these pathways intersect. Harding et al. identify an innate immune signaling mechanism initiating from damaged mitochondria via the NF-κB effector NEMO. In HeLa cells, mitochondrial NEMO recruitment is Parkin-dependent, and NF-κB activation occurs in parallel to mitochondrial clearance.

Graphical Abstract
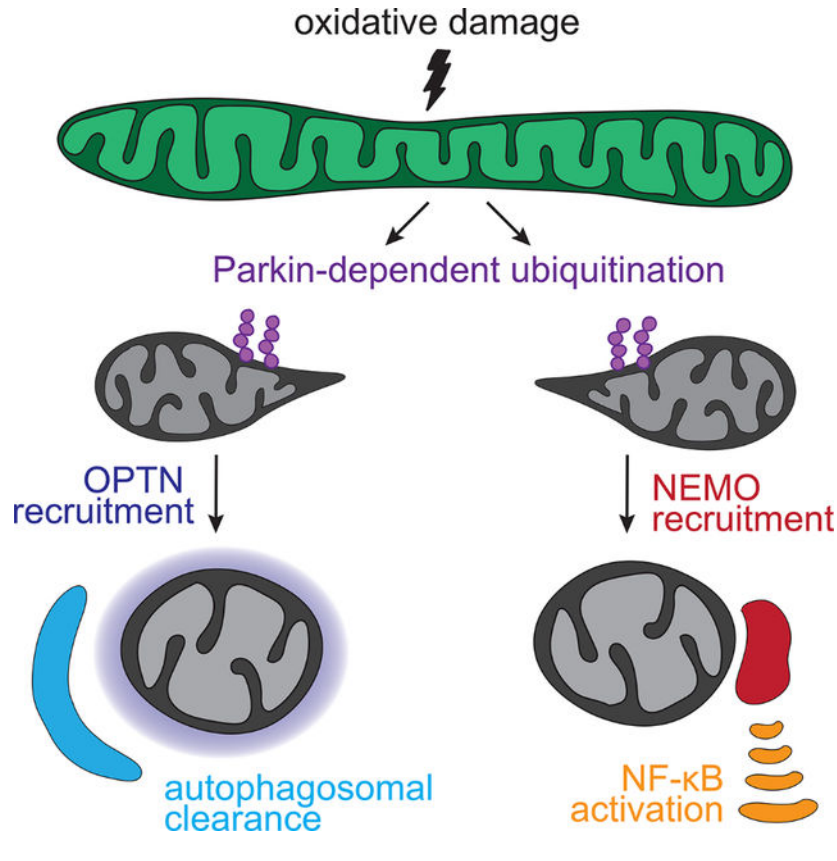
Introduction

The selective clearance of damaged mitochondria is induced by PINK1/Parkin-dependent mitophagy. Genes essential for this pathway are associated with neurodegenerative diseases including Parkinson's Disease (PD), amyotrophic lateral sclerosis (ALS), and frontotemporal dementia[1–3], suggesting that impaired mitochondrial clearance is deleterious for cellular health. During PINK1/Parkin-dependent mitophagy, ubiquitin is conjugated to proteins on the outer mitochondrial membrane (OMM), serving as an "eat-me" signal for sequestration and degradation[4–7]. Ubiquitination triggers the recruitment of ubiquitin-binding adaptors including Optineurin (OPTN) and p62/Sequestosome-1 (p62/SQSTM1)[8–11]. Adaptor recruitment promotes the formation of an isolation membrane by the core autophagy machinery, the ATGs[12,13]. Feed-forward mechanisms among mitophagy

adaptors, ATGs, and the growing double-membrane autophagosome ensure engulfment and sequestration of dysfunctional mitochondria[14–16].

Selective clearance is a conserved process that likely evolved as a mechanism to keep cells safe from harmful waste and invasive microorganisms[4–6,17,18]. Indeed, mitophagic mechanisms parallel xenophagy, the selective clearance of pathogens[19–21]. During xenophagy the cell may also activate innate immune pathways to communicate the presence of a threat, for example, cytosolic *Salmonella* induces the Nuclear Factor kappa B (NF-κB) pathway[19,20]. Damaged mitochondria may also initiate inflammatory warning signals, as neurodegenerative patients exhibit NF-κB pathway activation[22,23] and increased levels of cytokines in spinal sera[24,25].

Links between damaged mitochondria and inflammation have already been noted. Cytosolic mitochondrial DNA (mtDNA) is a damage-associated molecular pattern (DAMP) that activates cyclic GMP-AMP synthase-stimulator of interferon genes (cGAS-STING)[26,27]. Free mtDNA circulating in mitophagy-deficient *Pink1–/–;Prkn–/–* mouse sera may directly upregulate production of inflammatory cytokines, initiating or exacerbating degeneration[28]. It is also known that dysregulated mitochondrial production of reactive oxygen species (ROS) contributes to activation of the NLR family pyrin domain-containing 3 (NLRP3), which triggers the maturation of pro-inflammatory cytokines[29,30]. Non-autonomous innate immune mechanisms may also be mediated by mitochondria, as when cells respond to the cytokine Tumor Necrosis Factor Alpha (TNFα) by transforming the mitochondrial network into an amplification platform for NF-κB signaling[31]. The correlation between neuroinflammation and exacerbated degeneration suggests that abrogating immune responses in patients is a potential therapeutic strategy. However, small molecule inhibitors of inflammatory pathways have been unsuccessful in mitigating neurodegeneration to date. More investigation is necessary to identify the roots of inflammatory activation[32,33].

Here, we demonstrate that mitochondrial damage is sufficient to activate the classical NF-κB pathway via a Parkin-dependent mechanism. Following oxidative damage and the Parkin-dependent ubiquitination of OMM proteins, NF-κB Effector Molecule (NEMO) localizes to a subset of depolarized mitochondria with kinetics similar to recruitment of OPTN and p62. Pronounced NEMO puncta colocalize with p62, forming phase-separated bodies associated with the OMM. Rather than promoting mitochondrial clearance, NEMO recruitment triggers multimerization of the Inhibitor of kappa B kinase (IKK) complex, inducing auto-activation that results in the upregulation of NF-κB target genes. Strikingly, mitochondria that recruit NEMO lack the indicators of downstream clearance mechanisms such as phospho-OPTN and ATG8, suggesting that mitophagy and NF-κB signaling are divergent pathways. Consistent with activation of an inflammatory response, NEMO is recruited to mitochondria in primary astrocytes, suggesting NF-κB signaling may contribute to non-cell autonomous neuroinflammation in patients with PD and/or ALS.

Results

NEMO is recruited to damaged mitochondria in a Parkin-dependent manner

OPTN and NEMO share 64% homology in an α-helical Ubiquitin Binding domain in ABIN and NEMO (UBAN) domain (Figure 1A)[34,35]. The UBAN in OPTN is required for efficient recruitment to damaged mitochondria following PINK1-dependent activation of the E3-ubiquitin ligase Parkin, which induces the ubiquitination of proteins bound to the OMM[8,11]. The UBAN of NEMO is required for the recruitment to activated, poly-ubiquitinated TNFα receptor, TNFR1[36,37]. More recently, NEMO was shown to be recruited to ubiquitinated, cytosolic microorganisms, which act as a signaling platform[19,20]. Interactions of NEMO with poly-ubiquitin induce phase separation and activation of the catalytic IKK complex, permitting downstream NF-κB activation[38,39].

We hypothesized that given the homology between NEMO and OPTN, NEMO would be similarly recruited to the ubiquitinated OMM of damaged mitochondria. To test this, we expressed EGFP-NEMO[40] and the mitochondrial-targeted fluorophore Mito-dsRed2 along with Parkin in HeLa cells (Figure 1B, *left*), and used Antimycin A and Oligomycin A (AntA/OligA) to depolarize mitochondria[41]. Within 1 hr of AntA/OligA treatment, we observed NEMO puncta on depolarized, fragmented mitochondria (Figure 1B, *left, bottom*). This phenomenon was Parkin-dependent, as HeLa cells have very low levels of endogenous Parkin, and NEMO recruitment was not observed in HeLa cells not transfected with exogenous Parkin (Figure 1B, *right;* Figure 1C). There was a range of responses across cells, with up to 60% of mitochondria positive for NEMO in some cells and a less robust response in others (Figure 1D). The fraction of NEMO-positive mitochondria did not significantly increase from 1 to 2 hr after AntA/OligA treatment (Figure 1E). Importantly, we also observed the recruitment of endogenous NEMO to damaged, Parkin-positive mitochondria using immunocytochemistry (Supp Figure 1A). In both live and fixed cell assays the recruitment of NEMO to mitochondria was only observed following mitochondrial depolarization.

Next, we tracked individual recruitment events in Parkin-expressing cells using live cell spinning disk confocal microscopy (Figure 1F, Supp Movie 1). In most events, mitochondria gradually accrued NEMO puncta over a period of ~20 min (Figure 1F'). Rarely, however, a preexisting NEMO particle was recruited to the OMM, leading to a rapid, stepwise increase in fluorescence (Figure 1F"). Cytosolic NEMO particles were present at basal conditions in some cells (Figure 1B, *top left, arrow*) though they did not associate with the mitochondrial network prior to depolarization. Thus, *de novo* NEMO particle formation accounted for the majority of NEMO-positive mitochondria induced by AntA/OligA treatment.

The average time to half-maximal fluorescence intensity (half-max) was 30 ± 5 min post-AntA/OligA addition for EGFP-NEMO (Figure 1F), consistent with our hypothesis that NEMO is recruited by the Parkin-dependent conjugation of poly-ubiquitin on the OMM, which occurs within 30 min of damage[42]. Together, our data indicate that NEMO translocates to damaged mitochondria in a Parkin-dependent manner, where it forms puncta on the OMM that endure for up to 2 hr post damage.

NEMO recruitment parallels, but is independent of, the recruitment of the mitophagy adaptor OPTN

We next compared the recruitment of OPTN and NEMO to depolarized mitochondria in Parkin-expressing cells (Figure 2A,B): $18 \pm 3.5\%$ of mitochondria recruited only OPTN 1 hr after AntA/OligA addition, while $5.7 \pm 1.2\%$ recruited only NEMO, and $6.7 \pm 1.5\%$ recruited both OPTN and NEMO (Figure 2B). Thus, OPTN recruitment is more extensive than NEMO recruitment, while mitochondria may recruit either or both of these UBAN-containing proteins. NEMO occupancy was not correlated to Nuclear domain 10 protein 52 (NDP52), another mitophagy adaptor that complements OPTN in mitochondrial clearance downstream of Parkin activation[9] (Supp Figure 1B).

We compared the timing of OPTN and NEMO recruitment in live cells by analyzing events in which NEMO and OPTN were recruited to the same mitochondrion (Supp Movie 2) and found that neither protein was consistently recruited first (Figure 2C). It is likely that poly-ubiquitin on the OMM recruits both NEMO and OPTN, thus they are recruited in broadly similar time-courses; consistent with this interpretation we find that on average, NEMO recruitment occurs 2.0 ± 1.8 min before OPTN ($t_{\text{NEMO-OPTN}}$) (Figure 2D). However, since OPTN and NEMO are not associated with each other in the cytosol[43], their recruitment kinetics are not tightly correlated.

Next, we used Airyscan microscopy to assess the spatial relationship between OPTN and NEMO on individual mitochondria in fixed cells (Figure 2E). Again, some mitochondria acquired only OPTN or only NEMO (Figure 2E, *yellow box*). However, some mitochondria demonstrated recruitment of both OPTN and NEMO (Figure 2E, *blue box*). Notably, OPTN and NEMO did not overlap on these organelles but rather occupied discrete, often adjacent domains. Previous work utilizing super-resolution microscopy identified poly-ubiquitinated microdomains on the surface of cytosolic *Salmonella*[19]; our observations suggest the presence of analogous microdomains on depolarized mitochondria.

We asked whether OPTN and NEMO compete for binding to poly-ubiquitin on the OMM by testing whether NEMO would be more robustly recruited in HeLa cells that had been CRISPR-edited to knock out OPTN (*OPTN*–/–)[9] (Figure 2F). Upon treatment with AntA/OligA, NEMO was recruited to damaged mitochondria to a similar extent in cells with or without OPTN (Figure 2G). Together, these results indicate that the absence of OPTN does not permit a more extensive recruitment of NEMO to depolarized mitochondria, nor is OPTN required for NEMO recruitment.

NEMO and p62 interact and colocalize to condensates at the OMM of damaged mitochondria

We wondered whether the differential patterning of NEMO and OPTN on the OMM reflected the formation of ubiquitin microdomains on mitochondrial surface. There are varying reports on the type of ubiquitin chains that recruit NEMO, with K63 and M1 (linear) chains being the primary candidates. *In vitro*, NEMO interacts with both K63 and linear ubiquitin, with a preference for linear ubiquitin[35,36]. In cells, NEMO is recruited to cytosolic *Salmonella* ubiquitination catalyzed by the Linear Ubiquitin Chain Assembly

Complex (LUBAC)[19,20], while activated TNFR complexes that recruit NEMO are decorated with both linear and K63 types[44,45]. While TNFα treatment induced a significant increase in linear ubiquitin chains compared to cells treated with a vehicle control, AntA/OligA administration did not stimulate linear ubiquitination (Supp Figure 2A,B), corroborating previous ubiquitylomic data demonstrating little to no linear ubiquitination in response to mitochondrial damage[8,41]. As a further test, we depleted cells of a required catalytic component of LUBAC, heme-oxidized IRP2 ubiquitin ligase-1 (HOIL1) (Supp Figure 2C). Cells depleted of HOIL1 (siHOIL) showed no increase in linear ubiquitination over vehicle-treated controls following stimulation with TNFα, indicating a functional inhibition of LUBAC activity (Supp Figure 2A,B). However, the recruitment of NEMO to damaged mitochondria was not affected in cells treated with siHOIL (Supp Figure 2D). Together, these observations do not support a role for linear ubquitination in the recruitment of NEMO to damaged mitochondria, and instead indicate that NEMO recruitment is downstream of Parkin-conjugated ubiquitination.

We also investigated other possibilities that might predict NEMO localization. Activated PINK1 leads to phosphorylation of ubiquitin monomers at Serine 65 (S65); and phospho-S65-ubiquitin monomers are subsequently incorporated into Parkin-catalyzed chains[46]. We used an antibody to phospho-S65-ubiquitin to test whether NEMO microdomains were correlated to post-translationally modified ubiquitin on the OMM. Phospho-ubiquitin signal was abundant after 1 hr AntA/OligA treatment, however NEMO localization was not specific to OMM regions enriched with phospho-ubiquitin (Supp Figure 2E). Mitochondrial DNA (mtDNA) has been shown to activate the cGAS-STING pathway of interferon production upon escape from the mitochondrial matrix[26,27]. We asked whether sites of mtDNA escape correlated with NEMO puncta formation by immunolabeling double-stranded DNA. dsDNA was observed in cell nuclei and in mitochondria, but again, the presence of dsDNA did not correlate with NEMO puncta (Supp Figure 2F).

Instead, we noted that the localization of NEMO to fragmented, ubiquitinated mitochondria was reminiscent of p62 recruitment: NEMO often adopts a bar-like formation between adjacent rounded mitochondria (Figure 2E, *blue box*) much like p62 localization to the interstices of damaged mitochondria[11,47]. We co-expressed Parkin, EGFP-NEMO, and mCherry-p62 in HeLa cells CRISPR-edited to knock out p62 (*p62–/–*)[48] and found that overexpressed NEMO and p62 formed perinuclear puncta in cells under basal conditions that sometimes appeared to colocalize, though they did not associate with the filamentous mitochondrial network (Figure 3A,B, "vehicle"). In contrast, in cells treated with AntA/OligA for 1 hr, NEMO and p62 demonstrated striking colocalization to fragmented mitochondria, with puncta both more numerous and more prominent compared to cells in basal conditions (Figure 3A,B, "AntA/OligA"). We found the same colocalization of EGFP-NEMO with endogenous p62 in wild-type HeLa cells after mitochondrial depolarization (Supp Figure 3A,B).

We used live imaging to analyze the recruitment kinetics of p62 and NEMO (Figure 3C, Supp Movie 3). Unlike the wide variance in t between NEMO and OPTN recruitment (Figure 2D), NEMO and p62 were recruited with very similar kinetics, exhibiting a much smaller variance among events (-1.6 ± 1.1 min) (Figure 3D). While preexisting cytosolic

puncta may occasionally be recruited to damaged mitochondria (Figure 1F"), *de novo* formation accounted for the majority of puncta seen on the OMM. Thus, NEMO and p62 recruitment to depolarized mitochondria are correlated in space and time.

To further probe interactions between NEMO and p62, we purified GFP-NEMO (Supp Figure 3C,D)[49]. Purified GFP-NEMO robustly associated with mCherry-p62 bound to RFP-Trap beads (Figure 3E, *left column*). NEMO also associated with p62 in the presence of soluble poly-ubiquitin (GST-4XUB) (Figure 3E, *middle column*), but neither NEMO nor p62 fluorescence was affected by the addition of GST-4XUB (Figure 3F). Free NEMO and p62 individually associated with GSH beads coated with GST-4XUB, and were also recruited to GST-4XUB beads (Figure 3G), but neither enhanced the recruitment of the other (Figure 3H). While these studies support a direct interaction between NEMO and p62, the association was not preserved in co-immunoprecipitation assays from cell extracts (Supp Figure 3E,F). p62 demonstrated a high degree of non-specific binding (Supp Figure 3E, *top panel*) but was not enriched on beads prepared from cells expressing EGFP-NEMO compared to those from cells expressing an EGFP vector, in AntA/OligA or vehicle control conditions (Supp Figure 3F).

Thus, p62 and NEMO associate with each other and with poly-ubiquitin *in vitro* at molecular concentrations that mimic physiologically relevant concentrations[50], but these interactions are likely transient, dynamic, and low affinity, as they were not preserved through the co-immunoprecipitation assay. These observations prompted us to ask whether NEMO and p62 together form phase separated condensates with a high liquid-liquid exchange to the surroundings, as had been previously shown individually for NEMO[38,39] and p62[47,51]. We administered 1,6-hexanediol to live, AntA/OligA-treated cells and observed the rapid dissolution of EGFP-NEMO particles associated with fragmented mitochondria (Figure 4A), an effect consistent with phase separation[52,53]. We attempted to identify instances of fission or fusion of mitochondrial NEMO particles, as has been previously shown for phase separated NEMO[38,39], however we suspect NEMO tethering to ubiquitinated OMM reduces condensate motility, making fission and fusion events rare.

To assess the nature of the particles more directly, we performed fluorescence recovery after photobleaching (FRAP) assays on live cells co-expressing EGFP-NEMO and mCherry-p62 (Figure 4B), as phase separated condensates should rapidly recover fluorescence after targeted photobleaching due to exchange with the cytosolic pool. Both EGFP-NEMO and mCherry-p62 fluorescence recovered following photobleaching, with fluorescence recovery of EGFP-NEMO by 3 min and mCherry-p62 fluorescence by a slower average of ~6 min (Figure 4A,B). The difference in recovery times may be due to a higher propensity for overexpressed mCherry-p62 to aggregate[54], impairing recovery time. EGFP-NEMO fluorescence recovered with similar dynamics regardless of the presence of mCherry-p62 (Supp Figure 4A). Together, these data indicate that ubiquitination of depolarized mitochondria transforms these organelles into platforms that host molecular assemblies of NEMO and p62 that undergo rapid exchange with the microenvironment.

When we depleted endogenous p62 with a targeted siRNA, we observed the loss of visible NEMO puncta on damaged mitochondria after damage (Supp Figure 4B–D). The PB1

domain of p62 is required for p62 phase separation, and the UBA-type UBD domain is required to recruit p62 to poly-ubiquitinated domains where its phase separation is catalyzed[47,51]. By expressing a series of mCherry-tagged p62 variants (Supp Figure 4E,F) in *p62–/–* cells[55,56], we determined that visible NEMO puncta formation was dependent on the PB1 and UBA domains of p62 (Supp Figure 4G). Deletions or inhibitory point mutations of these domains, but not of the TNF Receptor Associated Factor 6 (TRAF6)-interacting (TIR) or LC3-interacting (LIR) regions diminished the percent of mitochondria exhibiting robust NEMO puncta (Supp Figure 4G). Each mCherry-tagged p62 variant was expressed to the same extent in *p62–/–* cells (Supp Figure 4H), and the recruitment of OPTN was not affected by expression of any of the p62 variants (Supp Figure 4F, *left column*).

We did not see the recruitment of large NEMO puncta to damaged mitochondria in cells with transient depletion of p62 by siRNA (Supp Figure 4B–D) nor in p62 knockout cells (Supp Figure 4F,G). However, NEMO recruitment to damaged mitochondria could still be observed in *p62–/–* cells using an antibody to GFP to enhance the signal (Figure 4D, Supp Figure 4I). Thus, while p62 oligomerization and recruitment enhance robust formation of EGFP-NEMO-positive condensates at the OMM, p62 expression was not necessary for NEMO recruitment.

To confirm that ubiquitination of damaged mitochondria was sufficient for NEMO localization, we expressed a NEMO construct in which a conserved residue in the UBAN domain was mutated from aspartic acid to asparagine (NEMO^{D304N}), disrupting the ability of NEMO to establish electrostatic interactions with poly-ubiquitin[36,37] (Figure 4E). NEMO^{D304N} or NEMO^{WT} were expressed at equivalent levels (Supp Figure 4J); however, recruitment of NEMO^{D304N} was impaired compared to NEMO^{WT} recruitment (Figure 4E,F), indicating that the NEMO's UBAN was required to facilitate maximal recruitment. The residual recruitment of NEMO observed in NEMO^{D304N}-expressing cells may be attributed to homodimerization of the ubiquitin-binding mutant NEMO^{D304N} with endogenous, wild-type NEMO. Alternatively, the ZnF domain of NEMO (Figure 1A) may mediate poly-ubiquitin recognition to some extent[57]. However, the significantly decreased recruitment of NEMO^{D304N} as compared to NEMO^{WT} in AntA/OligA conditions indicates that the ZnF domain is not sufficient to drive NEMO association with poly-ubiquitinated mitochondria to the same degree.

Mitochondrial subpopulations that recruit NEMO or OPTN have distinct fates

As OPTN and NEMO were most frequently recruited to distinct mitochondrial subpopulations following oxidative damage (Figure 2E), we asked if these subpopulations undergo distinct fates. OPTN phosphorylation is catalyzed by TANK-binding kinase 1 (TBK1) and Unc-like Autophagy Activating Kinase 1 (ULK1), and is required for efficient clearance of damaged mitochondria[42,58,59]. We used an antibody specific for OPTN phosphorylated at serine-177 (pOPTN), and found that Parkin-expressing cells that had undergone depolarization damage exhibited many pOPTN-positive mitochondria (Figure 5A). Notably, these mitochondria tended to be distinct from the population of mitochondria that recruited NEMO (Figure 5B), with only a small fraction of mitochondria recruiting both.

We then asked whether NEMO recruitment was also negatively correlated with markers of downstream steps of mitophagy, such as the recruitment of the ATG8 family proteins required for the formation of the autophagosomal membrane[15,60]. In both selective and non-selective autophagy, assembly of ATG8-positive membranes indicates engulfment of cellular material for degradation[60]. We probed Parkin-expressing cells with an antibody recognizing the ATG8 family members GABARAP, GABARAPL1, and GABARAPL2 (GABARAPs) and found that after mitochondrial depolarization, only a small population (<10%) of fragmented mitochondria were positive for both NEMO and GABARAPs; instead, almost half of mitochondria were positive for either NEMO or the ATG8s while half recruited neither at this time point (Figure 5C,D). This result was consistent with a parallel experiment in which we measured recruitment of NEMO and another ATG8, LC3B (Supp Figure 5A,B). The partitioning of mitochondria into sub-populations that recruited either NEMO or markers of downstream clearance suggests that some mitochondria maintain persistent NEMO localization and are not engulfed by autophagosomes.

Next, we examined Parkin-expressing cells up to 5 hr after mitochondrial depolarization in order to examine later stages of mitophagy without triggering cell death pathways[61] (Figure 5E,F). Mitochondrial content makes up ~18% of total cell area under basal conditions; this did not significantly decrease after 1 hr AntA/OligA treatment (Figure 5F, *top left*), though many fragmented mitochondria were encircled by Halo-OPTN rings (Figure 5E). After 5 hr of treatment, mitochondrial area decreased by half to ~9% of total cell area (Figure 5F, *top left*), as damaged mitochondria were engulfed and degraded by autophagosomes. The Mito-dsRed2 signal was lost while OPTN rings were reduced to fluorescent puncta, as the Halo-ligand remains stable in the acidic milieu of lysosomes [62]. Of note, by 5 hr of depolarization, the percent of remaining mitochondria positive for NEMO was significantly increased from basal conditions (Figure 5F, *top right*). Therefore, mitochondria not cleared by 5 hr were more likely to be NEMO-positive. The proportion of mitochondria positive for OPTN also increased by 5 hr, which was expected since the mitophagy pathway continued to progress in this time span (Figure 5F, *bottom left*). However, even 5 hr after mitochondrial damage, we did not see any evidence of increased overlap between OPTN and NEMO (Figure 5F, *bottom right*). Together, these data suggest differential fates for mitochondria that recruit OPTN or NEMO; OPTN-associated mitochondria are more likely to undergo mitophagy, while NEMO-associated mitochondria are more likely to persistently accumulate following mitochondrial depolarization.

The activated IKK complex promotes NF-κB signaling from damaged mitochondria

NEMO is an essential regulator of classical NF-κB signaling, one of three subunits that comprise the IKK complex. The two other subunits, IKKα and IKKβ, are kinases activated via phosphorylation induced by multi-IKK complexing and phase separation[38,39,63,64]. In order to determine whether IKKβ is co-recruited to damaged mitochondria with NEMO, we co-expressed NEMO with a fluorescently tagged construct of IKKβ[65] in the presence of Parkin (Figure 6A). Upon mitochondrial depolarization, there was colocalization of NEMO and IKKβ at fragmented mitochondria, indicating IKK multi-complex formation (Figure 6A, *bottom*). We also found that endogenous IKKβ was recruited to damaged mitochondria by immunostaining fixed cells (Supp Figure 6A).

The binding of NEMO to poly-ubiquitin chains induces phase separation of the IKK complex and conformational changes among the IKK subunits, both of which promote IKKβ phosphorylation and complex activation[38,39,63]. Since our 1,6-hexanediol and FRAP results suggest that NEMO forms phase-separated bodies at the OMM (Figure 4A,B), we posited that these condensates would activate IKK signaling. We probed fixed cells with an antibody to phospho-Ser176/pSer180-IKKα/β (pIKK) and found that mitochondria positive for NEMO recruitment also demonstrated evidence of activated IKK (Figure 6B) and that pIKK intensity was significantly higher in AntA/OligA-treated Parkin-expressing cells (Figure 6C). Together these data suggest that NEMO is co-recruited to the same damaged mitochondria as are catalytic IKK components, and the complex is activated via phosphorylation.

In canonical NF-κB signaling, and in signaling transmitted from cytosolic *Salmonella*, active IKK induces nuclear translocation of NF-κB transcription factors[19,20]. Given the recruitment and activation of the IKK complex at damaged mitochondria, we asked whether NF-κB target genes were upregulated in the context of Parkin-dependent mitophagy. We isolated mRNA from cells in basal conditions or after AntA/OligA treatment and performed RT-qPCR to detect the levels of transcripts encoding the pro-inflammatory cytokines TNFα and interleukin 6 (IL6). AntA/OligA-treated cells produced significantly higher levels of *TNFA*- and *IL6*-transcripts in a Parkin-dependent manner (Figure 6D). In cells without exogenous Parkin, AntA/OligA increased *IL6* transcripts relative to basal conditions, however mitochondrial depolarization in Parkin-expressing cells resulted in significantly higher levels of *IL6* (Figure 6D). Upregulation of NF-κB genes was also dependent on NEMO expression, as cells depleted of endogenous NEMO demonstrated suppressed levels of *TNFA* (Figure 6E, Supp Figure 6B). In contrast, we did not find evidence of induction of an interferon-type response program characterized by upregulation of antiviral transcript *IFIT3* in response to mitochondrial damage (Figure 6D,E). Production of *TNFA* and *IL6* is consistent with induction of an innate immune response that promotes microglial activation and proliferation[66], features documented repeatedly in patients with neurodegeneration[67,68]. The lack of *IFIT* upregulation corroborates our finding that cells are not undergoing a cGAS-STING response to cytosolic mtDNA in the context of our assays (Supp Figure 2F)[26]. In keeping with our previous results demonstrating NEMO recruitment in the absence of p62 (Figure 4D), the Parkin-dependent AntA/OligA-induced cytokine response did not require expression of p62, as *TNFA* and *IL6* were upregulated after AntA/OligA depolarization in *p62−/−* cells (Supp Fig 6C).

Damaged mitochondria induce NEMO/NF-κB signaling in astrocytes

Finally, we sought to test whether NEMO recruitment to damaged mitochondria would be recapitulated in physiologically relevant cell types. We first asked whether mitochondrial depolarization in neurons would activate cell-autonomous innate immune signaling. We used an antibody to assess the localization of endogenous NEMO in primary hippocampal neurons expressing a SNAP-tagged mitochondrial targeting sequence (Mito-SNAP). AntA disrupted the mitochondrial network within 1 hr, resulting in fragmented mitochondrial morphology. However, in both vehicle-treated and AntA-treated neurons, NEMO demonstrated baseline mitochondrial localization with no induction following

depolarization (Supp Figure 6D). This outcome suggests that mitochondrial damage does not induce NF-κB signaling from mitophagy intermediates in neurons to a similar level as seen in HeLa cells.

Astrocytes are implicated in the exacerbation of several diseases with a neuroinflammatory component. In ALS, astrocytes produce factors that are directly toxic to motor neurons[69], and in murine models of PD, blocking astrocyte activation is protective[70]. Furthermore, astrocytes exhibit high levels of PINK1 expression and activation[71]. Thus, we tested whether NEMO recruitment to damaged mitochondria could be recapitulated in murine astrocytes. We cultured primary astrocytes[72] and induced mitochondrial stress with 10 μM AntA and 5 μM OligA or a vehicle control for 2 hours. AntA/OligA-treated astrocytes displayed severe mitochondrial fragmentation as expected[71] (Figure 6F). We observed pronounced recruitment of endogenous NEMO to damaged mitochondria and measured significantly higher mitochondrial NEMO intensity in AntA/OligA-treated astrocytes (Figure 6F,G).

Together, data from relevant cell types suggested that NF-κB activation by mitophagy intermediates is a mechanism more pertinent to astrocytes than neurons. This disparity may be because PINK1/Parkin-dependent mitochondrial ubiquitination in neurons is insufficient to induce the robust recruitment of NEMO[41], while ubiquitination in astrocytes is more robust. Together, our data demonstrate a mechanism by which depolarized mitochondria in astrocytes recruit the NF-κB effector NEMO and suggest that this recruitment may promote inflammatory signaling.

Discussion

Mitochondria have been frequently implicated in innate immunity, with evidence ranging from ontology studies linking mitochondrial quality control genes to autoimmune diseases, to the discovery that mtDNA is a Damage-Associated Molecular Pattern (DAMP). Here, show that damaged mitochondria in Parkin-expressing cells become intracellular platforms that initiate NF-κB signaling via NEMO recruitment, simultaneous to the recruitment of OPTN and activation of mitophagy (Figure 6H). Our model is reminiscent of *Salmonella* Typhimurium invasion of the cytosol, in which ubiquitin microdomains on the exposed bacterial surface recruit both xenophagic clearance elements and the IKK complex, activating NF-κB signaling[19,20]. In the case of cytosolic bacteria, autophagosomal clearance and NF-κB activation are independently important to cell health and viability. In contrast, given that mitochondrial dysfunction and neuroinflammation are hallmarks of neurodegenerative disease, we propose that chronic activation of the mitochondrial signaling paradigm elaborated may be deleterious and may contribute to progressive degeneration.

NEMO and OPTN are each recruited to fragmented mitochondria, but segregate by microdomains on the OMM or by subpopulation of mitochondria. The topography of ubiquitin linkages on the OMM may contribute to the specificity or stability of OPTN or NEMO occupancy. Parkin ligase activity generates mainly K63 chains[41], however, longer or shorter chains may result in preferential recruitment of various adaptors; more work is required to explore this finding.

Importantly, NEMO-positive mitochondria are cleared more slowly by ATG8-positive phagophores (Figure 5). Although previous studies have shown that OPTN can out-compete NEMO for poly-ubiquitinated Receptor-Interacting Protein (RIP) at the TNFR1[43], we found that NEMO recruitment was not amplified by depletion of OPTN (Figure 2F,G). Instead, we noted that there is a "ceiling" for NEMO recruitment to the OMM of damaged mitochondria, which may be due to ubiquitin chain specificity, p62 condensates, or another unidentified factor specific to the mitophagy context. It may be beneficial for cells to limit mitochondrial accumulation of NEMO in order to dampen downstream inflammatory signaling. While damaged mitochondria undergo lysosomal degradation over time, NEMO-positive mitochondria persist >5 hr post-depolarization. We hypothesize that the chronic localization of NEMO prolongs NF-κB signaling and upregulation of cytokine expression. Other mediators of classic NF-κB signaling such as TAK1 and TAB1/2 may also be recruited (Kehl et al. 2019; Adhikari et al. 2007).

p62-NEMO interactions have not been previously reported in the context of mitochondrial clearance, although tandem mass tag spectrometry to determine ubiquitinated targets in a Dox-inducible Parkin system identified OPTN and TBK1 among the highly ubiquitinated targets within 1 hr of AntA/OligA treatment. After 6 hr, p62 and NEMO were highly ubiquitinated, while the other adaptors were less represented in the sample pool[6]. This could indicate that a portion of mitochondria not cleared in the first 6 hr after depolarization accumulate NEMO and p62. Meanwhile, NEMO and p62 interactions have been documented in studies of NF-κB activation upon TNFα and IL-1β stimulation[73]. Interestingly, TNFα exposure can also initiate LUBAC recruitment to the mitochondrial network, where it catalyzes linear ubiquitination of NEMO and promotes NF-κB shuttling to the nucleus[31]. While we did not find a requirement for LUBAC in the pathway presented here (Supp Figure 2A–D), *TNFA* upregulation initiated by mitochondrial depolarization may result in non-cell-autonomous signaling and further amplification of the inflammatory program.

The potential for mitophagy intermediates to evoke NEMO-mediated NF-κB signaling has implications for dysfunctional clearance pathways associated with neurodegeneration. Parkin is expressed in neural cell types, including neurons, microglia, and astrocytes[74,75], and loss of function mutations in both *PINK1* and *PRKN* genes cause adult-onset PD[76], suggesting that Parkin-mediated mitophagy is a critical homeostatic mechanism for the brain. The failure to observe damage-induced increases in NEMO localization in neurons (Supp Figure 6D) may be due to lower levels of ubiquitination by endogenous Parkin in this cell type. Although the types of ubiquitination are comparable between neurons and HeLa cells, the abundance of ubiquitin on mitochondrial substrates is lesser by an order of magnitude in neurons [41]. In contrast, astrocytes demonstrated high PINK1 activity and pronounced levels of phosphorylated ubiquitin in a study of endogenous proteins in mouse brains[71]. Consistent with this finding, we found that primary astrocytes exhibited robust recruitment of NEMO in response to oxidative damage, though we did not test Parkin-dependence in this model (Figure 6F,G). NEMO-mediated NF-κB signaling in astrocytes could then lead to upregulation of cytokines, as seen in the cerebrospinal fluid of patients with neurodegenerative disease [24]. Further studies in both neurons and glia are required to understand the implications of mitophagic dysfunction in disease-related pathways in vivo.

It is also important to note that NF-κB signaling is crucial to cell survival pathways, promoting the expression of anti-apoptotic proteins such as calbindin and Bcl-2 family members[77]. Parkin-dependent NEMO recruitment and subsequent IKK activation may thus serve as a built-in brake to neuronal death pathways triggered by mitochondrial failure[78]. In PD patients with Parkin deficiency, Parkin-independent clearance pathways may be sufficient to stave off deleterious effects initially, but over a lifetime, an absence of NEMO signaling might also contribute to degeneration and/or cell death. NEMO-mediated pathways for inflammation and cell survival are likely tightly regulated, in the context of invasive bacteria or the malfunction of our resident bacterial descendants, mitochondria[20,79]. Any such signaling activated by mitophagy intermediates must be accounted for as we investigate underlying mechanisms of neurodegenerative pathology.

Limitations of the study

Our study focused on the molecular mechanisms that drive cell-autonomous initiation of innate immune signaling via mitophagy intermediates using a HeLa cell model. We found evidence of NF-κB activation upon mitochondrial depolarization, however we did not introduce disease-specific components to the model, such as neurodegeneration-related mutations in OPTN, TBK1 or p62. In the future it will be critical to understand how genetic perturbation of the pathway may modulate NEMO/IKK signaling. Additionally, though we saw NEMO recruitment to damaged astrocytic mitochondria, we did not confirm the Parkin-dependent nature of the mechanism in this cell type. Astrocytes were identified as a PINK1-expressing neural cell[71], but further work must demonstrate that NF-κB activation is dampened with PINK1 and/or Parkin depletion in this model. Then, studies may focus on the complexity of cell non-autonomous effects of mitochondrial-damage-mediated NF-κB activation and the possibility of a feedforward mechanism in which the depolarization-induced upregulation and secretion of TNFα then leads to further enhancement of NEMO-dependent IKK activation, as recently described by Wu et al.[31]. Such investigations may reveal more precise targets for therapeutic development.

STAR Methods

Resource availability

Lead Contact—Further information and requests for resources and reagents should be directed to and will be fulfilled by the lead contact, Erika L.F. Holzbaur (holzbaur@pennmedicine.upenn.edu)

Materials availability—Plasmids generated in this study have been deposited to Addgene.

Data and code availability

- All data, including Western blot images have been deposited at Zenodo and are publicly available as of the date of publication. DOI is listed in the key resources table.

- This paper does not report original code.

- Any additional information required to reanalyze the data reported in this paper is available from the lead contact upon request.

Experimental model and study participant details

Mammalian cell culture—HeLa-M[80]; HeLa-*OPTN*–/–[9]; and HeLa-*p62*–/–[48] are variants of HeLa cell line (female) and were maintained in Dulbecco's modified eagle medium (DMEM) with 10% fetal bovine serum (Hyclone) and 1% GlutaMAX glucose supplement (Gibco, Cat# 35050061) at 37°C with 5% CO_2. Passage number was below 30 for HeLa-M cells and below 20 for knock-out lineages. Each line was authenticated by STR profiling and tested for mycoplasma regularly.

Primary mouse astrocytes—Astrocytes were isolated and maintained as described in method details from cortices of pooled littermates of healthy P1-P3 C57BL6/J mice not used in any previous procedures. Each litter comprised a single replicate, thus, sex of astrocytes was mixed.

Primary rat hippocampal neurons—Hippocampal neurons were isolated from CD Sprague Dawley IGS rat embryos dissected at gestational day 18 from healthy adult females. Embryos were pooled for collection; thus, sex of neurons was mixed.

Escherichia coli: pLysS *E. coli* Rosetta (DE3) were maintained according to product instructions and transformed as described in method details.

Method details

Reagent generation—A human mitochondrial targeting sequence was recloned into pSBFP2-C1 and pSNAP$_f$ vectors to generate Mito-SBFP2 and Mito-SNAP. EGFP-NEMO[D304N] and Halo-NEMO were constructed using EGFP-mNEMO. pGEX-GST-NEMO was used for purified protein assays by inserting the GFP cassette via Gibson cloning after the Thrombin cleavage site. mCherry-p62-TIR[AAA] was generated by site-directed mutagenesis of mCherry-p62[WT].

Immortal cell culture and transfection—18–20 hours prior to fixation, live imaging, or collection, cells were approximately 80–90% confluent, and were transfected with the appropriate constructs using Lipofectamine 2000 (ThermoFisher Scientific, Cat# 11668027). For p62 knockdown, cells were transfected with 20 μM sip62 or a scrambled control and other constructs when they were 80–90% confluent and collected or imaged 40–48 hr post-transfection. For all other knockdowns, cells were transfected with 40 μM siRNA or a scrambled control using Lipofectamine RNAiMax (ThermoFisher Scientific, Cat# 13778100) when they were 50–60% confluent, 48 hr before imaging or collection.

Primary cell culture and transfection.—A suspension of embryonic day 18 Sprague Dawley rat hippocampal neurons was provided from the Neurons R Us Culture Service Center at the University of Pennsylvania. Cells were plated at a density of 250,000 cells/dish, on 35 mm glass-bottom dishes (MatTek) precoated with 0.5 mg/ml poly-L-lysine (Sigma Aldrich). Cells were initially plated in MEM supplemented with 10% horse

serum, 33 mM D-glucose, and 1 mM sodium pyruvate for 2–5 hours. The media was then replaced with Neurobasal (Gibco) supplemented with 33 mM D-glucose, 2 mM GlutaMAX (Invitrogen), 100 units/ml penicillin, 100 units/ml streptomycin, and 2% B-27 (ThermoFisher) (Maintenance Media; MM) and cells were maintained at 37C in a 5% CO_2 incubator. AraC (1 μM) was added the day after plating to prevent glia cell proliferation. Neurons were transfected at 5 days in vitro with DNA (0.8–1.2 μg of total plasmid) using Lipofectamine 2000 Transfection Reagent (ThermoFisher) and incubated 48 hours. Murine astrocytes were isolated based on the protocol detailed in Schildge et al.[72]. Briefly, cortices from C57BL/6J mice (P1-P3) were removed, mechanically dissociated, and digested in 2.5% trypsin for 10 minutes at 37°. Cells were then pelleted at 2.0 gxs for 4 minutes, washed 3x in astrocyte maintenance media (high glucose DMEM with pyruvate, ThermoFisher, cat #11995065, 10% FBS, 1% Penicillin/Streptomycin) and plated on Poly-D-Lysine (PDL)-coated flasks (ThermoFisher, Cat# A3890401). To procure an astrocyte-enriched culture, cells were shaken at 250 rpm for 6 hours, washed twice in PBS, and passed onto PDL-coated, glass-bottom imaging dishes using trypsin-EDTA (Life Technologies, Cat# 25300054). Astrocytes were treated as detailed and immediately fixed 6–9 days post-plating.

Labeling and treatment for on live cells—To label Halo-tagged proteins, cells were incubated with 190 nM Halo ligand in media for at least 20 min. For SNAP-tagged proteins, cells were incubated with 1.25 μM SNAP ligand in media for at least 45 min. For depolarization (or vehicle control), immortalized cells and astrocytes were treated with a combination of 5 μM Oligomycin A (or DMSO) and 10 μM Antimycin A (or EtOH). In hippocampal neurons, additional MM was added to 35-mm dishes for a final working concentration of 35 nM Antimycin A for 1 hr.

Fixation—Immortal cells were fixed with 4% paraformaldehyde (PFA). Hippocampal neurons and astrocytes were fixed with 4% PFA with addition of 4% sucrose, weight/volume. For imaging of autophagosomes (GABARAPs and LC3B), after PFA fixation cells were permeabilized in methanol and blocked in 5% goat serum (Fisher Scientific, Cat# G9023), 1% BSA. For staining pIKK and IKKβ, after PFA fixation cells were permeabilized with 0.2% Triton-X and blocked in 10% FBS in DMEM[81]. For all other immortal lines, cells were permeabilized in 0.5% Triton-X and blocked with 3% BSA, 0.2% Triton-X. Astrocytes were permeabilized in 0.25% Triton-X in PBS and blocked in 5% goat serum, 1% BSA in PBS. Cells were incubated with primary antibodies overnight.

Cell Microscopy—For live cell imaging, conditioned media was replaced with Leibovitz's L-15 Medium (Gibco, Cat# 11415064) supplemented with 10% fetal bovine serum. Fields of view were chosen to maximize the number of healthy-appearing cells that expressed detectable components of interest. All samples except where indicated as AiryScan or widefield were imaged with a Nikon Eclipse Ti Microscope with a 60X objective (Apochromat, Nikon, 1.40-N.A. oil immersion) or 100X objective (Apochromat, Nikon, 1.49-N.A. oil immersion) and an UltraView Vox spinning disk confocal system (PerkinElmer) with a CMOS ORCA-Fusion camera (Hamamatsu, Cat# C11440–20UP). Z-stacks were collected for all samples except timelapses. The parameters for Z-stacks were 0.15 μm/step through at least 3.1 μm of cells' midsections or 0.2 μm/step through the volume

of each cell for astrocytes. Timelapse imaging was collected for confocal sections at 5 sec/frame for 1,6-Hexanediol experiment and 60 sec/frame for others. For timelapse imaging with the addition of AntA/OligA or 1,6-Hexanediol, 5–10 frames were collected prior to addition, then a volume of imaging media at least 50% of the initial volume was added, including AntA/OligA, to bring the total concentration to 10 μM AntA/5 μM OligA or 5% 1,6-Hexanediol as frame collection continued. For fluorescence recovery assay, NEMO puncta were outlined with a region of interest (ROI) and imaged every 5 s. Three frames were collected before ROIs underwent 1 cycle of photobleaching at 18 ms per pixel, then imaging continued for a total of 10 min. Volocity or Visiview were used as acquisition software for confocal images. For widefield detection (Supp Figures 4H, 6B), images were collected with a Leica CTR7000 HS Microscope with a 40X objective (Leica, 1.25-N.A. oil immersion) and captured with a Hamamatsu ORCA R^2 digital CCD camera (C10600–10B). Leica Application Suite X was used as acquisition software. For AiryScan detection, fixed samples were imaged with a Zeiss Axio Observer inverted microscope with a 63X objective (oil immersion). Data were collected with ZEN software.

Co-immunoprecipitations and immunoblots—For standard cell lysis, cells were lysed with RIPA buffer (50 mM Tris-HCl, 1 mM EDTA, 2 mM EGTA, 1% Triton X, 0.5% sodium deoxycholate, 0.1% sodium dodecyl sulfate, 150 mM NaCl) with added Halt Protease and Phosphatase Inhibitor Cocktail (ThermoFisher Scientific, Cat#78444) and assayed for protein concentration with Pierce BCA Protein Assay Kit (ThermoFisher Scientific, Cat#23225). For EGFP-NEMO immunoprecipitation, cells were lysed by freeze-thaw and suspended in buffer as described previously [82]. GFP-Trap Magnetic Particles (Chromotek Cat#M-270) were used to immunoprecipitate GFP conjugated elements. All samples were assayed by SDS-PAGE and labeled with fluorescent secondary antibodies (Li-Cor) for imaging on an Odyssey CLx machine (Li-Cor).

Protein purification—GFP-NEMO was expressed in *E. coli* Rosetta (DE3) pLysS cells. Cells were grown at 37 °C to an OD600 of 0.6, when they reached an OD600 of 0.8 at 18 °C they were induced with 0.1 mM isopropyl β-D-1-thiogalactopyranoside, and grown for additional 16 h at 18 °C. Cells were harvested by centrifugation, flash frozen and stored at −80 °C. For purification the pellet was thawed and resuspended in lysis buffer (50 mM HEPES pH 7.5, 300 mM NaCl, 2 mM $MgCl_2$, 2 mM β-mercaptoethanol, Roche Protease Inhibitor, DNAse I (Sigma) and 1 mM DTT), sonicated three times (30 sec, 5 cycles, 65% power) and centrifuged for 45 minutes at 20,000 rpm. The supernatant was filtered through a 0.45 μm syringe filter and incubated on equilibrated Glutathione Sepharose 4B beads (GE Healthcare) at 4 °C. After 4 hours the beads were washed 5 times with wash buffer 1 (50 mM HEPES pH 7.5, 300 mM NaCl, 1 mM DTT), once with wash buffer 2 (50 mM HEPES pH 7.5, 700 mM NaCl, 1 mM DTT) and again twice with wash buffer 1. GFP-NEMO was cleaved with thrombin overnight, filtered through a 0.45 μm syringe filter and concentrated to a final volume of 500 μL using 10 kDa MWCO concentrator (Millipore), before being further purified by size exclusion chromatography on a Superose 6 Increase 10/300 column (GE Healthcare) in 25 mM HEPES pH 7.5, 150 mM NaCl, 1 mM DTT.

Protein-protein interaction assay microscopy—Microscopy-based protein-protein interaction assays were performed as described previously [82]. Briefly, Glutathione Sepharose 4B beads (GE Healthcare) or RFP-Trap Agarose beads (ChromoTek), with an average diameter of 90 μm, were saturated with GST-tagged or mCherry-tagged bait proteins (5 uM) by incubation at 4 °C for 1 hour. Beads were then washed twice with washing buffer (25 mM HEPES pH 7.5, 150 mM NaCl, 1 mM DTT) and resuspended in washing buffer (1:1). 1 μM prey proteins were mixed with bait-coupled beads in the microscopy plate. After 30 min incubation at room temperature beads were imaged at the equilibrium by Zeiss LSM 700 confocal microscope equipped with Plan-Apochromat 20X/0.8 objective.

RNA extraction and RT-qPCR—~One million cells were collected for each condition after 5 hr incubation with vehicle control or AntA/OligA using standard TRIzol protocol (ThermoFisher, Cat# 15596026) to extract RNA. cDNA was generated using the SuperScript First-Strand Synthesis System (ThermoFisher, Cat# 11904018). cDNA was cleaned using Zymo Research Oligo Clean & Concentrator kit (Cat# D4060). 11 ng samples or equivalent of nuclease free water for No Transcript Control were added to each reaction with 300 nM of each primer. PowerUP SYBR Green Master Mix (Applied Biosystems, Cat# A25742) was used to catalyze PCR in a QuantStudio 3 Real-Time PCR System Machine (Applied Biosystems, Cat# A28567). Amplification data was produced with QuantStudio Design and Analysis software.

Image processing and data analysis.—Microscopy images were deconvolved where indicated with Huygen's Professional software to remove background noise and increase resolution and signal-to noise ratio. The Classic Maximum Likelihood Estimation (CMLE) algorithm with theoretical PSF was performed for up to 60 iterations. The signal-to-noise ratio for all channels was set between 10 and 30, depending on the individual construct; all other settings were default. Deconvolved images are not scaled to intensity where displayed. 2 μm max projections were made where indicated to account for the approximate volume of a fragmented mitochondrion. For "Proportion of cells with NEMO recruitment" quantification, each cell was cropped from its respective field, max projected, and blinded with other cells in the experimental set. Blinded cells were scored as demonstrating NEMO recruitment or not. For most "% Mitochondria with [protein] recruited" analysis, deconvolved, max-projected images were trained with Ilastik software [83] and binary images were generated for the respective particles (Mito, NEMO, etc.). FIJI/ImageJ [84] was used to determine overlap between particles, and percentages were calculated from the fraction of NEMO or OPTN particles overlapping mitochondria to total mitochondria. GABARAPs-positive and LC3B-positive mitochondria were identified by hand due to the low signal-to-noise ratio for the antibodies. For quantification of intensity over time, events were chosen to quantify if they remained within the z plane for most of the sequence. ROIs were manually drawn around the fragmented mitochondrion for each time frame. Intensities for NEMO and/or others were measured for each ROI. Five-frame averages were taken to smooth intensity measurements, and background was calculated from the mean intensity in the respective channel for the first 10 frames and subtracted from every time point. Finally, each intensity measurement was normalized to the maximal intensity recorded for that channel for that event to produce "% of Max Intensity". For astrocyte quantification, masks of

mitochondria were generated from max-projected Mic60 images by performing a rolling ball background subtraction, followed by Otsu thresholding and despeckling if needed. Following, ROIs procured from mitochondrial masks were superimposed onto NEMO images to measure mean intensity of NEMO fluorescence overlapping with mitochondria. Quantification of microscopy-based protein-protein interaction assays was performed in ImageJ2 (version 2.3.0/1.53f). A maximum Z-projection of the acquired stack was made and the intensity of the signal around the beads was measured by drawing a line across each bead and recording the maximum intensity value along the line. Values were background-corrected by subtracting the average intensity of a region of the image field with no beads. The corrected values for each sample were averaged between three independent replicates and plotted with the standard deviations. For immunoblots, ImageStudio Software was used to scan bands to ensure no patches were overexposed. ImageStudio was then used to subtract background and quantify band intensities as described. Values were graphed and analyzed in GraphPad software, except for Euler plots, which were created using RStudio. Images were assembled in Adobe Illustrator.

Quantification and statistical analysis

Statistical details for each analysis can be found in the figure legend corresponding to the data displayed. Analyses were performed using GraphPad Prism. At least 3 independent experiments were performed for every dataset; significance was determined using a confidence interval of 95%.

Supplementary Material

Refer to Web version on PubMed Central for supplementary material.

Acknowledgements

Inclusion and Diversity

We support inclusive, diverse, and equitable conduct of research.

References

1. Abramzon YA, Fratta P, Traynor BJ, and Chia R (2020). The Overlapping Genetics of Amyotrophic Lateral Sclerosis and Frontotemporal Dementia. Front. Neurosci. 14, 1–10. 10.3389/fnins.2020.00042. [PubMed: 32038151]

2. Cirulli ET, Lasseigne BN, Petrovski S, Sapp PC, Dion PA, Leblond CS, Couthouis J, Lu Y-F, Wang Q, Krueger BJ, et al. (2015). Exome sequencing in amyotrophic lateral sclerosis identifies risk genes and pathways. Science (80–.). 347, 1436–1441.

3. Chang D, Nalls MA, Hallgrímsdóttir IB, Hunkapiller J, van der Brug M, Cai F, Kerchner GA, Ayalon G, Bingol B, Sheng M, et al. (2017). A meta-analysis of genome-wide association studies identifies 17 new Parkinson's disease risk loci. Nat. Genet. 49, 1511–1516. 10.1038/ng.3955. [PubMed: 28892059]

4. Goodall EA, Kraus F, and Harper JW (2022). Mechanisms underlying ubiquitin-driven selective mitochondrial and bacterial autophagy. Mol. Cell, 1–13. 10.1016/j.molcel.2022.03.012. [PubMed: 34995505]

5. Pohl C, and Dikic I (2019). Cellular quality control by the ubiquitin-proteasome system and autophagy. Science (80–.). 366, 818–822. 10.1126/science.aax3769.

6. Rose C, Isasa M, Ordureau A, Prado MA, Beausoleil SA, Jedrychowski MP, Finley DJ, Harper JW, and Gygi S (2016). Highly Multiplexed Quantitative Mass Spectrometry Analysis of Ubiquitylomes. Cell Syst. 3, 395–403. [PubMed: 27667366]

7. Narendra D, Tanaka A, Suen DF, and Youle RJ (2008). Parkin is recruited selectively to impaired mitochondria and promotes their autophagy. J. Cell Biol. 183, 795–803. 10.1083/jcb.200809125. [PubMed: 19029340]

8. Heo J-M, Ordureau A, Paulo JA, Rinehart J, and Harper JW (2015). The PINK1-PARKIN Mitochondrial Ubiquitylation Pathway Drives a Program of OPTN/NDP52 Recruitment and TBK1 Activation to Promote Mitophagy. Mol. Cell 60, 7–20. 10.1016/j.molcel.2015.08.016.. [PubMed: 26365381]

9. Lazarou M, Sliter DA, Kane LA, Sarraf SA, Wang C, Burman JL, Sideris DP, Fogel AI, and Youle RJ (2015). The ubiquitin kinase PINK1 recruits autophagy receptors to induce mitophagy. Nature 524, 309–314. 10.1038/nature14893. [PubMed: 26266977]

10. Pickles S, Vigié P, and Youle RJ (2018). Mitophagy and Quality Control Mechanisms in Mitochondrial Maintenance. Curr. Biol. 28, R142–R143. 10.1016/j.cub.2018.01.004. [PubMed: 29462575]

11. Wong YC, and Holzbaur ELF (2014). Optineurin is an autophagy receptor for damaged mitochondria in parkin-mediated mitophagy that is disrupted by an ALS-linked mutation. Proc. Natl. Acad. Sci. U. S. A. 111, E4439–E4448. 10.1073/pnas.1405752111. [PubMed: 25294927]

12. Valverde DP, Yu S, Boggavarapu V, Kumar N, Lees JA, Walz T, Reinisch KM, and Melia TJ (2019). ATG2 transports lipids to promote autophagosome biogenesis. J. Cell Biol. 218, 1787–1798. 10.1083/jcb.201811139. [PubMed: 30952800]

13. Rogov V, Dötsch V, Johansen T, and Kirkin V (2014). Interactions between autophagy receptors and ubiquitin-like proteins form the molecular basis for selective autophagy. Mol. Cell 53, 167–178. 10.1016/j.molcel.2013.12.014. [PubMed: 24462201]

14. Vargas JNS, Wang C, Bunker E, Hao L, Maric D, Schiavo G, Randow F, and Youle RJ (2019). Spatiotemporal Control of ULK1 Activation by NDP52 and TBK1 during Selective Autophagy. Mol. Cell 74, 1–16. 10.1016/j.molcel.2019.02.010. [PubMed: 30951649]

15. Turco E, Fracchiolla D, and Martens S (2020). Recruitment and Activation of the ULK1/Atg1 Kinase Complex in Selective Autophagy. J. Mol. Biol. 432, 123–134. 10.1016/j.jmb.2019.07.027. [PubMed: 31351898]

16. Chang C, Shi X, Jensen L, Yokom A, Dorotea F, Sascha M, and H., H.J. (2022). Reconstitution of cargo-induced LC3 lipidation in mammalian selective autophagy. Sci. Adv. 7, eabg4922. 10.1126/sciadv.abg4922.

17. Manifava M, and Ktistakis NT (2022). Chapter 24 - Autophagy on the road to longevity and aging. In Autophagy in Health and Disease (Second Edition), Rothermel BA and T.-A. AB in H. and D. (Second Diwan E, eds. (Academic Press), pp. 347–360. 10.1016/B978-0-12-822003-0.00002-4.

18. Stolz A, Ernst A, and Dikic I (2014). Cargo recognition and trafficking in selective autophagy. Nat. Cell Biol. 16, 495–501. 10.1038/ncb2979. [PubMed: 24875736]

19. Noad J, Von Der Malsburg A, Pathe C, Michel MA, Komander D, and Randow F (2017). . LUBAC-synthesized linear ubiquitin chains restrict cytosol-invading bacteria by activating autophagy and NF-kBNat. Microbiol. 2. 10.1038/nmicrobiol.2017.63.

20. Van Wijk SJL, Fricke F, Herhaus L, Gupta J, Hötte K, Pampaloni F, Grumati P, Kaulich M, Sou Y-S, Komatsu M, et al. (2017). Linear ubiquitination of cytosolic Salmonella Typhimurium activates NF-κB and restricts bacterial proliferation. Nat. Microbiol. 2. 10.1038/nmicrobiol.2017.66.

21. Wild P, Farhan H, McEwan D, Wagner S, Rogov V, Brady N, Richter B, Korac J, Waidmann O, Choudhary C, et al. (2011). Phosphorylation of the Autophagy Receptor Optineurin Restricts Salmonella Growth. Science (80–.). 333, 228–233. 10.1126/science.1203466. [PubMed: 21617041]

22. Swarup V, Phaneuf D, Dupre N, Petri S, Strong M, Kriz J, and Julien J-P (2011). Deregulation of TDP-43 in amyotrophic lateral sclerosis triggers nuclear factor B–mediated pathogenic pathways. J. Exp. Med 208, 2429–2447. 10.1084/jem.20111313. [PubMed: 22084410]

23. Amor S, Peferoen LAN, Vogel DYS, Breur M, van der Valk P, Baker D, and van Noort JM (2014). Inflammation in neurodegenerative diseases-an update. Immunology 142, 151–166. 10.1111/imm.12233. [PubMed: 24329535]

24. Hu Y, Cao C, Qin X-Y, Yu Y, Yuan J, Zhao Y, and Cheng Y (2017). Increased peripheral blood inflammatory cytokine levels in amyotrophic lateral sclerosis: a meta-analysis study. Sci. Rep. 7. 10.1038/s41598-017-09097-1.

25. Nagatsu T, Mogi M, Ichinose H, and Togari A (2000). Cytokines in Parkinson's disease. J. Neural Transm. Suppl., 143–151.

26. West AP, Khoury-Hanold W, Staron M, Tal MC, Pineda CM, Lang SM, Bestwick M, Duguay BA, Raimundo N, MacDuff DA, et al. (2015). Mitochondrial DNA stress primes the antiviral innate immune response. Nature 520, 553–557. 10.1038/nature14156. [PubMed: 25642965]

27. Yu C-H, Davidson S, Harapas CR, Hilton JB, Mlodzianoski MJ, Laohamonthonkul P, Louis C, Low RRJ, Moecking J, De Nardo D, et al. (2020). TDP-43 Triggers Mitochondrial DNA Release via mPTP to Activate cGAS/STING in ALS. Cell 183, 636–649.e18. 10.1016/j.cell.2020.09.020. [PubMed: 33031745]

28. Sliter DA, Martinez J, Hao L, Chen X, Sun N, Fischer TD, Burman JL, Li Y, Zhang Z, Narendra DP, et al. (2018). Parkin and PINK1 mitigate STING-induced inflammation. Nature 561, 258–262. 10.1038/s41586-018-0448-9. [PubMed: 30135585]

29. Sarkar S, Malovic E, Harishchandra DS, Ghaisas S, Panicker N, Charli A, Palanisamy BN, Rokad D, Jin H, Anantharam V, et al. (2017). Mitochondrial impairment in microglia amplifies NLRP3 inflammasome proinflammatory signaling in cell culture and animal models of Parkinson's disease. npj Park. Dis. 3. 10.1038/s41531-017-0032-2.

30. Zhou R, Yazdi AS, Menu P, and Tschopp J (2011). A role for mitochondria in NLRP3 inflammasome activation. Nature 496, 221–225. 10.1038/nature09663.

31. Wu Z, Berlemann LA, Bader V, Sehr DA, Dawin E, Covallero A, Meschede J, Angersbach L, Showkat C, Michaelis JB, et al. (2022). LUBAC assembles a ubiquitin signaling platform at mitochondria for signal amplification and transport of NF-κB to the nucleus. EMBO J. 41. 10.15252/embj.2022112006.

32. Fournier CN, Schoenfeld D, Berry JD, Cudkowicz ME, Chan J, Quinn C, Brown RH, Salameh JS, Tansey MG, Beers DR, et al. (2018). An open label study of a novel immunosuppression intervention for the treatment of amyotrophic lateral sclerosis. Amyotroph. Lateral Scler. Front. Degener. 19, 242–249. 10.1080/21678421.2017.1421666.

33. Wang Q, Liu Y, and Zhou J (2015). Neuroinflammation in Parkinson's disease and its potential as therapeutic target. Transl. Neurodegener. 4. 10.1186/s40035-015-0042-0.

34. Li F, Xie X, Wang Y, Liu J, Cheng X, Guo Y, Gong Y, Hu S, and Pan L (2016). Structural insights into the interaction and disease mechanism of neurodegenerative disease-associated optineurin and TBK1 proteins. Nat. Commun. 7. 10.1038/ncomms12708.

35. Yoshikawa A, Sato Y, Yamashita M, Mimura H, Yamagata A, and Fukai S (2009). Crystal structure of the NEMO ubiquitin-binding domain in complex with Lys 63-linked di-ubiquitin. FEBS Lett. 583, 3317–3322. 10.1016/j.febslet.2009.09.028. [PubMed: 19766637]

36. Rahighi S, Ikeda F, Kawasaki M, Akutsu M, Suzuki N, Kato R, Kensche T, Uejima T, Bloor S, Komander D, et al. (2009). Specific Recognition of Linear Ubiquitin Chains by NEMO Is Important for NF-κB Activation. Cell 136, 1098–1109. 10.1016/j.cell.2009.03.007.. [PubMed: 19303852]

37. Wu C-J, Conze DB, Li T, Srinivasula SM, and Ashwell JD (2006). Sensing of Lys 63-linked polyubiquitination by NEMO is a key event in NF-κB activation. Nat. Cell Biol. 8, 398–406. 10.1038/ncb1384. [PubMed: 16547522]

38. Du M, Ea C, Fang Y, and Chen ZJ (2022). Liquid phase separation of NEMO induced by polyubiquitin chains activates NF- kB Graphical abstract. Mol. Cell, 1–12. 10.1016/j.molcel.2022.03.037.

39. Goel S, Oliva R, Jeganathan S, Bader V, Krause LJ, Kriegler S, Stender ID, Christine CW, Nakamura K, Hoffmann JE, et al. (2023). Linear ubiquitination induces NEMO phase separation to activate NF-κB signaling. Life Sci. alliance 6, 1–18. 10.26508/lsa.202201607.

40. Tarantino N, Tinevez JY, Crowell EF, Boisson B, Henriques R, Mhlanga M, Agou F, Israël A, and Laplantine E (2014). Tnf and il-1 exhibit distinct ubiquitin requirements for inducing NEMO-IKK supramolecular structures. J. Cell Biol. 204, 231–245. 10.1083/jcb.201307172. [PubMed: 24446482]

41. Ordureau A, Paulo JA, Zhang W, Ahfeldt T, Zhang J, Cohn EF, Hou Z, Heo J-M, Rubin LL, Sidhu SS, et al. (2018). Dynamics of PARKIN-Dependent Mitochondrial Ubiquitylation in Induced Neurons and Model Systems Revealed by Digital Snapshot Proteomics. Mol. Cell 70, 1–17. [PubMed: 29625031]

42. Moore AS, and Holzbaur ELF (2016). Dynamic recruitment and activation of ALS-associated TBK1 with its target optineurin are required for efficient mitophagy. Proc. Natl. Acad. Sci. U. S. A. 113, E3349–E3358. 10.1073/pnas.1523810113. [PubMed: 27247382]

43. Zhu G, Wu C-J, Zhao Y, and Ashwell JD (2007). Optineurin Negatively Regulates TNFa- Induced NF-kB Activation by Competing with NEMO for Ubiquitinated RIP. Curr. Biol. 17, 1438–1443. 10.1016/j.cub.2007.07.041. [PubMed: 17702576]

44. Lafont E, Draber P, Rieser E, Reichert M, Kupka S, de Miguel D, Draberova H, von Mässenhausen A, Bhamra A, Henderson S, et al. (2018). TBK1 and IKKε prevent TNF-induced cell death by RIPK1 phosphorylation. Nat. Cell Biol. 20, 1389–1399. 10.1038/s41556-018-0229-6. [PubMed: 30420664]

45. Ea C-K, Deng L, Xia Z-P, Pineda G, and Chen ZJ (2006). Activation of IKK by TNFα Requires Site-Specific Ubiquitination of RIP1 and Polyubiquitin Binding by NEMO. Mol. Cell 22, 245– 257. 10.1016/j.molcel.2006.03.026. [PubMed: 16603398]

46. Okatsu K, Oka T, Iguchi M, Imamura K, Kosako H, Tani N, Kimura M, Go E, Koyano F, Funayama M, et al. (2012). PINK1 autophosphorylation upon membrane potential dissipation is essential for Parkin recruitment to damaged mitochondria. Nat. Commun. 3, 1016. 10.1038/ ncomms2016. [PubMed: 22910362]

47. Sun D, Wu R, Zheng J, Li P, and Yu L (2018). Polyubiquitin chain-induced p62 phase separation drives autophagic cargo segregation. Cell Res. 28, 405–415. 10.1038/s41422-018-0017-7. [PubMed: 29507397]

48. Sarraf SA, Shah HV, Kanfer G, Pickrell AM, Holtzclaw LA, Ward ME, and Youle RJ (2020). Loss of TAX1BP1-Directed Autophagy Results in Protein Aggregate Accumulation in the Brain. Mol. Cell, 1–17. 10.1016/j.molcel.2020.10.041.

49. Ko MS, Biswas T, Mulero MC, Bobkov AA, Ghosh G, and Huxford T (2020). Structurally plastic NEMO and oligomerization prone IKK2 subunits define the behavior of human IKK2:NEMO complexes in solution. Biochim. Biophys. Acta - Proteins Proteomics 1868, 140526. 10.1016/ j.bbapap.2020.140526. [PubMed: 32853772]

50. Cho NH, Cheveralls KC, Brunner A-D, Kim K, Michaelis AC, Raghavan P, Kobayashi H, Savy L, Li JY, Canaj H, et al. (2023). OpenCell: Endogenous tagging for the cartography of human cellular organization. Science (80–.). 375, eabi6983. 10.1126/science.abi6983.

51. Zaffagnini G, Savova A, Danieli A, Romanov J, Tremel S, Ebner M, Peterbauer T, Sztacho M, Trapannone R, Tarafder AK, et al. (2018). P62 Filaments Capture and Present Ubiquitinated Cargos for Autophagy. EMBO J, e98308. 10.15252/embj.201798308. [PubMed: 29343546]

52. Kroschwald S, Maharana S, Mateju D, Malinovska L, Nüske E, Poser I, Richter D, and Alberti S (2015). Promiscuous interactions and protein disaggregases determine the material state of stress-inducible RNP granules. Elife 4, e06807. 10.7554/eLife.06807. [PubMed: 26238190]

53. Kageyama S, Gudmundsson SR, Sou YS, Ichimura Y, Tamura N, Kazuno S, Ueno T, Miura Y, Noshiro D, Abe M, et al. (2021). p62/SQSTM1-droplet serves as a platform for autophagosome formation and anti-oxidative stress response. Nat. Commun. 12. 10.1038/s41467-020-20185-1.

54. Lamark T, Perander M, Outzen H, Kristiansen K, Øvervatn A, Michaelsen E, Bjørkøy G, and Johansen T (2003). Interaction Codes within the Family of Mammalian Phox and Bem1p Domain-containing Proteins. J. Biol. Chem. 278, 34568–34581. 10.1074/jbc.M303221200. [PubMed: 12813044]

55. Wurzer B, Zaffagnini G, Fracchiolla D, Turco E, Abert C, Romanov J, and Martens S (2015). Oligomerization of p62 allows for selection of ubiquitinated cargo and isolation membrane during selective autophagy. Elife 4, 1–28. 10.7554/eLife.08941.

56. Jakobi AJ, Huber ST, Mortensen SA, Schultz SW, Palara A, Kuhm T, Shrestha BK, Lamark T, Hagen WJH, Wilmanns M, et al. (2020). Structural basis of p62/SQSTM1 helical filaments and their role in cellular cargo uptake. Nat. Commun. 11, 1–15. 10.1038/s41467-020-14343-8. [PubMed: 31911652]

57. Laplantine E, Fontan E, Chiaravalli J, Lopez T, Lakisic G, Véron M, Agou F, and Israël A (2009). NEMO specifically recognizes K63-linked poly-ubiquitin chains through a new bipartite ubiquitin-binding domain. EMBO J. 28, 2885–2895. 10.1038/emboj.2009.241. [PubMed: 19763089]

58. Harding O, S., E.C., Ye, J., Cheung, J., Maniatis, T., and Holzbaur, E.L.F. (2021). ALS- and FTD-associated missense mutations in TBK1 differentially disrupt mitophagy. Proc. Natl. Acad. Sci. 118, e2025053118. 10.1073/pnas.2025053118. [PubMed: 34099552]

59. Richter B, Sliter DA, Herhaus L, Stolz A, Wang C, Beli P, Zaffagnini G, Wild P, Martens S, Wagner SA, et al. (2016). Phosphorylation of OPTN by TBK1 enhances its binding to Ub chains and promotes selective autophagy of damaged mitochondria. PNAS 113, 4039–4044. 10.1073/pnas.1523926113. [PubMed: 27035970]

60. Tanida I, Ueno T, and Kominami E (2004). LC3 conjugation system in mammalian autophagy. Int. J. Biochem. Cell Biol. 36, 2503–2518. 10.1016/j.biocel.2004.05.009. [PubMed: 15325588]

61. Carroll RG, Hollville E, and Martin SJ (2014). Parkin Sensitizes toward Apoptosis Induced by Mitochondrial Depolarization through Promoting Degradation of Mcl-1. Cell Rep. 9, 1538–1553. 10.1016/j.celrep.2014.10.046. [PubMed: 25456142]

62. Yim WW-Y, Yamamoto H, and Mizushima N (2022). A pulse-chasable reporter processing assay for mammalian autophagic flux with HaloTag. Elife 11, e78923. 10.7554/eLife.78923. [PubMed: 35938926]

63. Ko MS, Cohen SN, Polley S, Mahata SK, Biswas T, Huxford T, and Ghosh G (2022). Regulatory subunit NEMO promotes polyubiquitin-dependent induction of NF-κB through a targetable second interaction with upstream activator IKK2. J. Biol. Chem. 298, 101864. 10.1016/j.jbc.2022.101864. [PubMed: 35339487]

64. Rushe M, Silvian L, Bixler S, Chen LL, Cheung A, Bowes S, Cuervo H, Berkowitz S, Zheng T, Guckian K, et al. (2008). Structure of a NEMO/IKK-Associating Domain Reveals Architecture of the Interaction Site. Structure 16, 798–808. 10.1016/j.str.2008.02.012. [PubMed: 18462684]

65. Birbach A, Gold P, Binder BR, Hofer E, de Martin R, and Schmid JA (2002). Signaling molecules of the NF-kappa B pathway shuttle constitutively between cytoplasm and nucleus. J. Biol. Chem. 277, 10842–10851. 10.1074/jbc.M112475200. [PubMed: 11801607]

66. Chiu IM, Morimoto ETA, Goodarzi H, Liao JT, O 'keeffe S, Phatnani HP, Muratet M, Carroll MC, Levy S, Tavazoie S, et al. (2013). A Neurodegeneration-Specific Gene-Expression Signature of Acutely Isolated Microglia from an Amyotrophic Lateral Sclerosis Mouse Model. Cell Rep. 4, 385–401. 10.1016/j.celrep.2013.06.018. [PubMed: 23850290]

67. Sitte HH, Wanschitz J, Budka H, and Berger ML (2001). Autoradiography with [3 H]PK11195 of spinal tract degeneration in amyotrophic lateral sclerosis. Acta Neuropathol. 101, 75–78. 10.1007/s004010000312. [PubMed: 11271375]

68. Philips T, and Robberecht W (2011). Neuroinflammation in amyotrophic lateral sclerosis: role of glial activation in motor neuron disease. Lancet Neurol. 10, 253–263. 10.1016/S1474-4422(11)70015-1. [PubMed: 21349440]

69. Haidet-Phillips AM, Hester ME, Miranda CJ, Meyer K, Braun L, Frakes A, Song S, Likhite S, Murtha MJ, Foust KD, et al. (2011). Astrocytes from familial and sporadic ALS patients are toxic to motor neurons. Nat. Biotechnol. 29, 824–828. 10.1038/nbt.1957. [PubMed: 21832997]

70. Yun SP, Kam T-I, Panicker N, Kim S, Oh Y, Park J-S, Kwon S-H, Park YJ, Karuppagounder S, Park H, et al. (2018). Block of A1 astrocyte conversion by microglia is neuroprotective in models of Parkinson's disease. Nat. Med. 24, 931–938. 10.1038/s41591-018-0051-5. [PubMed: 29892066]

71. Barodia SK, Mcmeekin LJ, Creed RB, Quinones EK, Cowell RM, and Goldberg MS (2019). PINK1 phosphorylates ubiquitin predominantly in astrocytes. npj Park. Dis. 5. 10.1038/s41531-019-0101-9.

72. Schildge S, Bohrer C, Beck K, and Schachtrup C (2013). Isolation and culture of mouse cortical astrocytes. J. Vis. Exp, 50079. 10.3791/50079.. [PubMed: 23380713]

73. Zotti T, Scudiero I, Settembre P, Ferravante A, Mazzone P, D'Andrea L, Reale C, Vito P, and Stilo R (2014). TRAF6-mediated ubiquitination of NEMO requires p62/sequestosome-1. Mol. Immunol. 58, 27–31. 10.1016/j.molimm.2013.10.015. [PubMed: 24270048]

74. Zhang Y, Sloan SA, Clarke LE, Caneda C, Plaza CA, Blumenthal PD, Vogel H, Steinberg GK, Edwards MSB, Li G, et al. (2016). Purification and Characterization of Progenitor and Mature Human Astrocytes Reveals Transcriptional and Functional Differences with Mouse. Neuron 89, 37–53. 10.1016/j.neuron.2015.11.013. [PubMed: 26687838]

75. Evans CS, and Holzbaur ELF (2019). Quality Control in Neurons: Mitophagy and Other Selective Autophagy Mechanisms. J. Mol. Biol. 432, 240–260. 10.1016/j.jmb.2019.06.031. [PubMed: 31295455]

76. Ge P, Dawson VL, and Dawson TM (2020). PINK1 and Parkin mitochondrial quality control: a source of regional vulnerability in Parkinson's disease. Mol. Neurodegener. 15, 1–18. 10.1186/s13024-020-00367-7. [PubMed: 31964406]

77. Mattson MP, Culmsee C, Yu Z, and Camandola S (2000). Roles of nuclear factor κB in neuronal survival and plasticity. J. Neurochem. 74, 443–456. 10.1046/j.1471-4159.2000.740443.x.. [PubMed: 10646495]

78. Henn IH, Bouman L, Schlehe JS, Schlierf A, Schramm JE, Wegener E, Nakaso K, Culmsee C, Berninger B, Krappmann D, et al. (2007). Parkin mediates neuroprotection through activation of IκB kinase/nuclear factor-κB signaling. J. Neurosci. 27, 1868–1878. 10.1523/JNEUROSCI.5537-06.2007. [PubMed: 17314283]

79. Youle RJ (2019). Mitochondria—Striking a balance between host and endosymbiont. Science (80–.). 365. 10.1126/science.aaw9855.

80. Caviston JP, Ross JL, Antony SM, Mariko T, and Holzbaur ELF (2007). Huntingtin facilitates dynein/dynactin-mediated vesicle transport. Proc. Natl. Acad. Sci. 104, 10045–10050. 10.1073/pnas.0610628104. [PubMed: 17548833]

81. Paul S, and Schaefer BC (2015). Visualizing TCR-Induced POLKADOTS Formation and NF-κB Activation in the D10 T-Cell Clone and Mouse Primary Effector T Cells. In NF-kappa B. Methods in Molecular Biology, May MJ, ed. (Humana Press), pp. 219–238. 10.1007/978-1-4939-2422-6_12.

82. Turco E, Witt M, Abert C, Bock-Bierbaum T, Su M-Y, Trapannone R, Sztacho M, Danieli A, Shi X, Zaffagnini G, et al. (2019). FIP200 Claw Domain Binding to p62 Promotes Autophagosome Formation at Ubiquitin Condensates. Mol. Cell 74, 1–17. 10.1016/j.molcel.2019.01.035. [PubMed: 30951649]

83. Berg S, Kutra D, Kroeger T, Straehle CN, Kausler BX, Haubold C, Schiegg M, Ales J, Beier T, Rudy M, et al. (2019). Ilastik: Interactive Machine Learning for (Bio)Image Analysis. Nat. Methods 16, 1226–1232. 10.1038/s41592-019-0582-9. [PubMed: 31570887]

84. Schindelin J, Arganda-Carreras I, Frise E, Kaynig V, Longair M, Pietzsch T, Preibisch S, Rueden C, Saalfeld S, Schmid B, et al. (2012). Fiji: An open-source platform for biological-image analysis. Nat. Methods 9, 676–682. 10.1038/nmeth.2019. [PubMed: 22743772]

Highlights

- Initiation of PINK1/Parkin mitophagy recruits NF-κB effector NEMO to mitochondria

- NEMO, p62, and OPTN are recruited in parallel to ubiquitinated mitochondria

- NEMO and p62 interact in phase condensates on the mitochondrial membrane

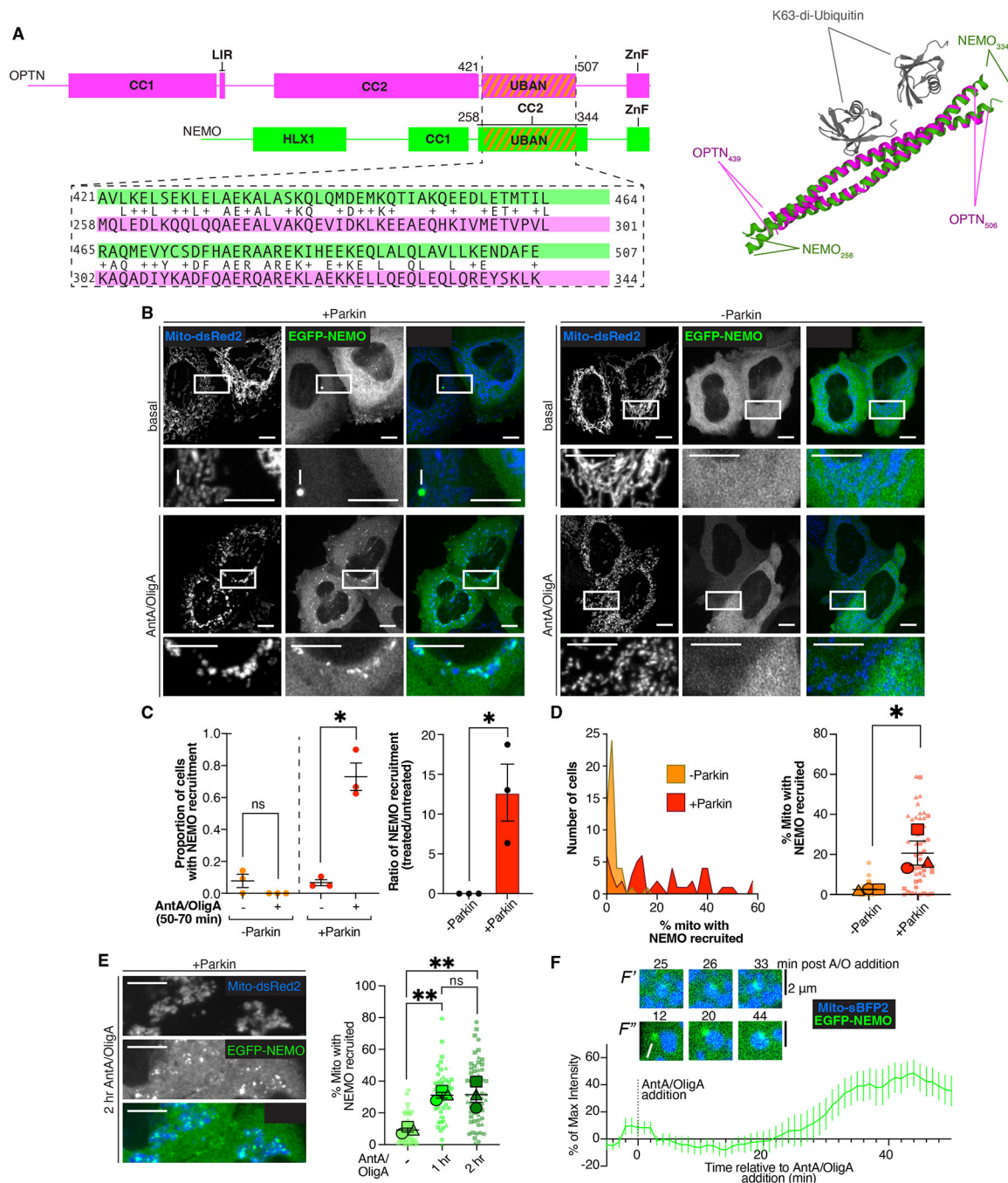- NEMO recruitment activates NF-κB signaling to induce cytokine expression

Figure 1. NEMO is structurally related to the mitophagy adaptor OPTN and is recruited to damaged mitochondria in a Parkin-dependent manner.
(A) Schematics of OPTN (pink) and NEMO (green); UBAN domains are highlighted with gold stripes. UBAN sequences of OPTN (pink) and NEMO (green) were aligned with NCBI BLAST. Small letters indicate exact matches. "+" indicates residues with chemical similarity. (Right) PDB pairwise structure alignment using jFATCAT (flexible) alignment between the UBAN domains of dimerized OPTN (PDB:5WQ4) (pink) and NEMO (PDB:3JSV) (green), and their interactions with K63-linked di-Ubiquitin (gray).

CC1/2, coiled coil domains; LIR, LC3 interacting region; ZnF, zinc-finger domain; HLX1, helical domain.

(B) Live HeLa cells expressing EGFP-NEMO and a mitochondria-targeted construct (Mito-dsRed2), with or without untagged Parkin at basal conditions (Top) or after 50–70 min treatment with 10 μM AntA/5 μM OligA. Arrow indicates punctum seen in basal condition. Arrowheads indicate fragmented mitochondria with NEMO recruited. Images deconvolved and max-projected 2 μm. (See Figure S1A.)

(C) (Left) Fraction of cells with NEMO recruitment in basal or AntA/OligA conditions. (Right) Ratio of AntA/OligA-treated versus basal conditions. Data from 3 independent experiments analyzed using paired t-tests (Left) or Welch's t-test (Right). Error bars indicate SEM; ns, not significant; *$P < 0.05$.

(D) Histogram of percent of NEMO-positive mitochondria by number of cells observed, and plot of percentage of NEMO-positive mitochondria. Data from 3 independent experiments analyzed using Welch's t-test. Error bars indicate SEM; *$P < 0.05$.

(E) HeLa cells expressing EGFP-NEMO, Mito-dsRed2, and untagged Parkin were fixed after 2 hr AntA/OligA treatment. Images max-projected 2 μm. (Right) NEMO occupancy on mitochondria in vehicle conditions, 1 hr, or 2 hr after AntA/OligA addition. Data from 3 independent experiments analyzed using one way ANOVA with multiple comparisons. Error bars indicate SEM; ns, not significant; **P 0.01.

(F) (*F' and F''*) Confocal images of live HeLa cells expressing a mitochondria-targeted BFP2 construct (Mito-sBFP2), EGFP-NEMO, and untagged Parkin over the course (min) of AntA/OligA treatment. In *F'*, arrowheads mark a gradually forming NEMO puncta. In *F''*, arrow marks a preexisting NEMO punctum near a mitochondrion. Arrowheads mark the subsequent interaction between the puncta and mitochondrion. (Below) Trace of average fluorescent intensity of NEMO recruited to mitochondria over time in 38 events following mitochondrial depolarization at 0 min. Data from 3 independent experiments. Error bars indicate SEM. (See Supp Movie 1).
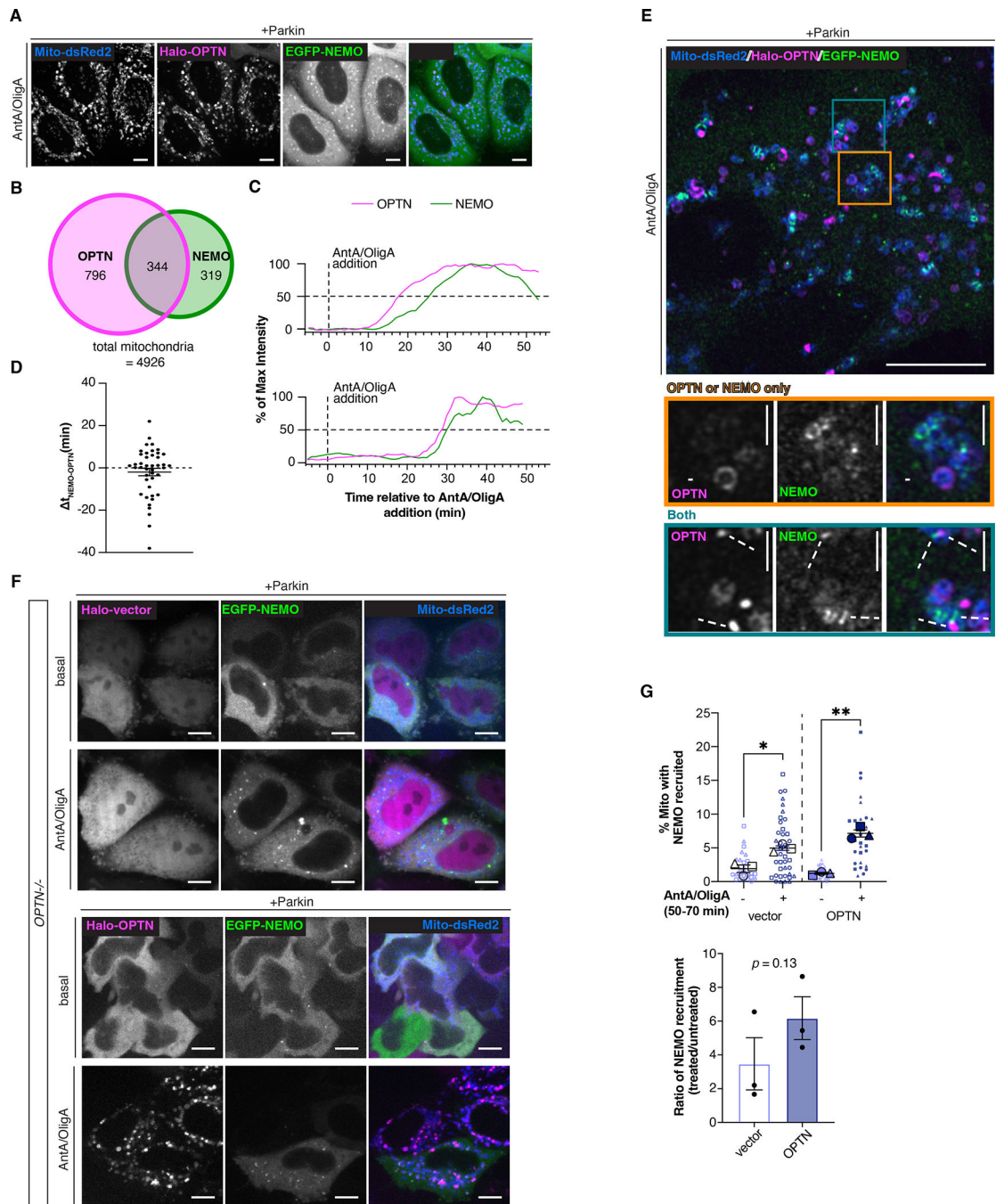
Figure 2. NEMO's interaction with mitochondria is distinct from OPTN.

(A) Live HeLa cells expressing EGFP-NEMO, Halo-OPTN, Mito-dsRed2, and untagged Parkin were treated with AntA/OligA for 50–70 min. Images max-projected 2 µm.

(B) Euler diagram demonstrating the raw number of mitochondria positive for OPTN, NEMO, or both. Remaining mitochondria were positive for neither.

(C) Example traces of the relative fluorescent intensities of OPTN and NEMO over time in 2 recruitment events. (See Supp Movie 2)

(D) Individual recruitment events were plotted by the difference (min) between NEMO and OPTN reaching their respective half-maximums ($t_{\text{NEMO-OPTN}}$). Data collected from 16 cells in 3 independent experiments. Error bars indicate SEM.

(E) Airyscan image of a fixed HeLa cell expressing EGFP-NEMO, Halo-OPTN, Mito-dsRed2, and untagged Parkin, treated with AntA/OligA for 60 min. Yellow box inset demonstrates examples in which only OPTN (Left arrow) or only NEMO (Right arrow) were recruited to mitochondria. Blue box inset demonstrates two examples in which both OPTN and NEMO were recruited to mitochondria (dotted line arrows).

(F) Live *OPTN–/–* cells expressing EGFP-NEMO, Mito-dsRed2 (Mito), untagged Parkin, and either Halo-vector or Halo-OPTN were imaged in basal conditions or after 50–70 min AntA/OligA treatment. Images max-projected 2 μm.

(G) (Top) Average percent of NEMO-positive mitochondria per cell in cells expressing Halo-vector or Halo-OPTN, in basal or AntA/OligA conditions. (Bottom) Ratios of (Top) plotted data, for treated versus control cells. Data from 3 independent experiments analyzed using (Top) paired t-tests or (Bottom) Welch's t-test. Error bars indicate SEM; *$P < 0.05$; **P 0.01.
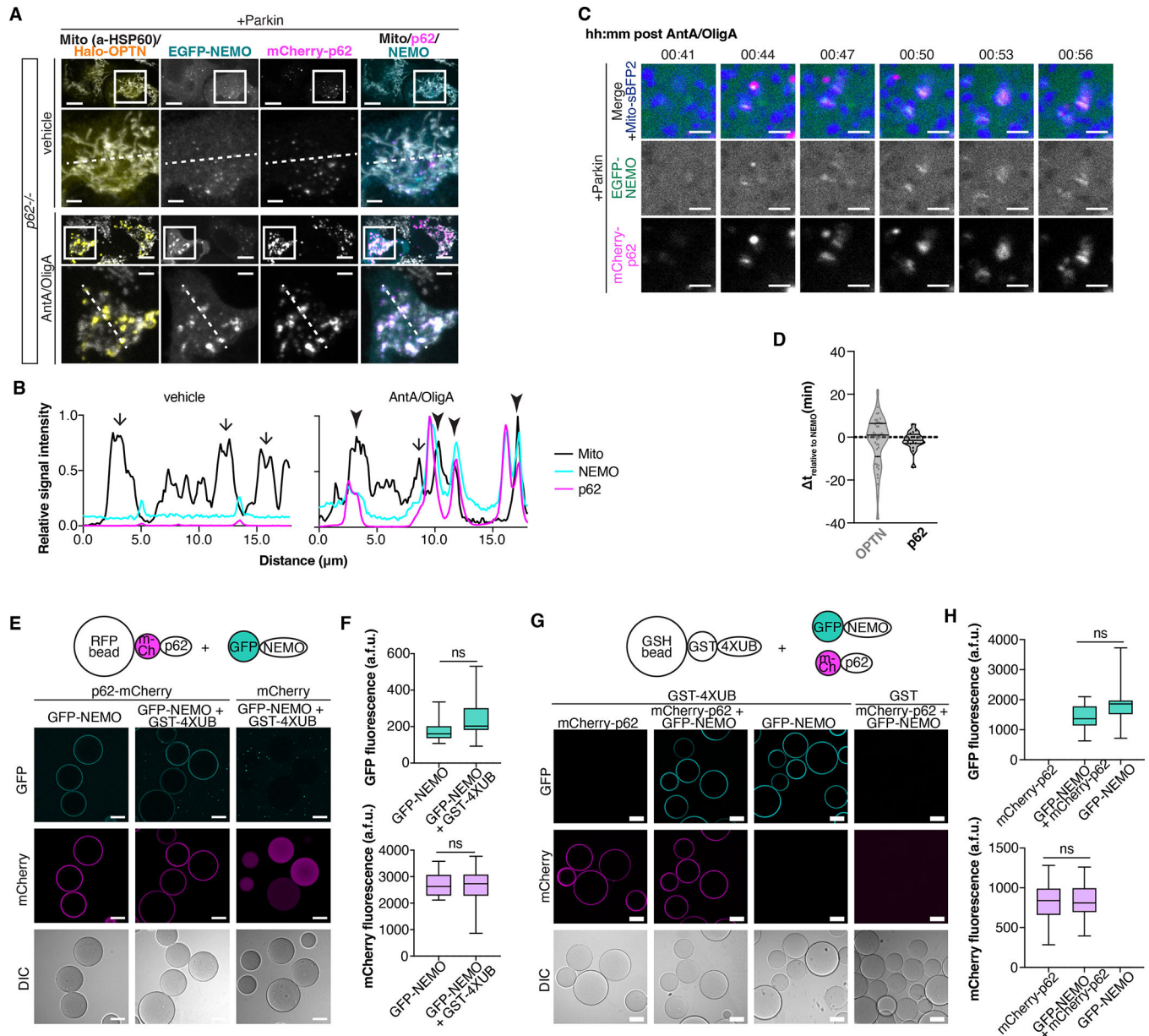
Figure 3. NEMO and p62 interact in vitro, and their recruitment to depolarized mitochondria are spatially and temporally linked.

(A) *p62–/–* cells expressing Halo-OPTN, EGFP-NEMO, mCherry-p62, and untagged Parkin were fixed after treatment in the respective conditions and labeled with antibodies to p62 and HSP60 (Mito). Dotted white line indicates where line scan data were collected (B). Images max-projected 2 μm. (See Figure S3A)

(B) Line scan of relative fluorescence intensities of Mito, NEMO, and p62 in (A). Arrows indicate mitochondria with no recruitment of NEMO or p62. Arrowheads indicate mitochondria with recruitment of colocalized NEMO and p62.

(C) Confocal images of live HeLa cells expressing a mitochondria-targeted BFP2 construct (Mito), EGFP-NEMO, mCherry-p62, and untagged Parkin over the course (hr:min) of AntA/

OligA treatment. Arrowheads mark 2 events in which p62 and NEMO were recruited to mitochondria. (See Supp. Movie 3)

(D) Individual recruitment events were plotted by the difference (minutes) between NEMO and OPTN (data copied from 2D) or NEMO and p62 reaching their respective half-maximums ($t_{relative\ to\ NEMO}$). Data for p62 recruitment were collected from six cells from 3 independent experiments. Solid lines within violin plots indicate median and first and third quartiles.

(E) Scheme and representative confocal images of microscopy-based pull-down showing the recruitment of GFP-NEMO (1 μM) in absence or presence of GST-4XUB (1 μM) to mCherry-p62 (5 μM) or mCherry (5 μM) coated RFP-trap beads. (See Figure S3C,D)

(F) Quantification of GFP (Top) and mCherry (Bottom) fluorescence as described in (E). Average GFP and mCherry signal intensities and standard deviations for 3 replicates are shown. Significance was tested through a nested ANOVA.

(G) Scheme and representative images of microscopy-based pull-down showing the recruitment of GFP-NEMO (1 μM) and/or mCherry-p62 (1 μM) to GST-4XUB (5 coated glutathione beads. Images were collected using a confocal microscopy.

(H) Quantification of GFP (Top) and mCherry (Bottom) fluorescence as described in (E). Average GFP and mCherry signal intensities and standard deviations for 3 replicates are shown. Significance tested through a nested ANOVA.
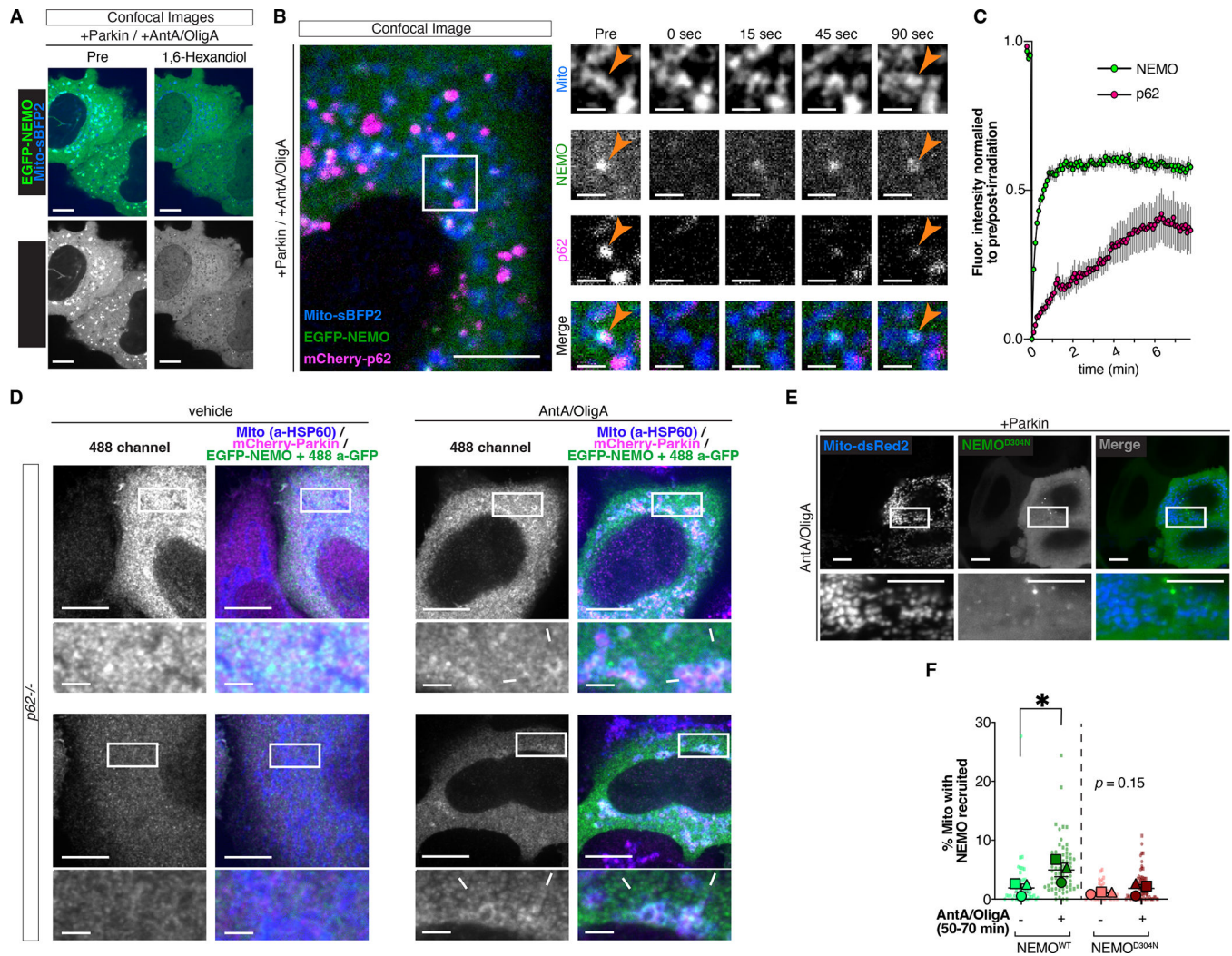
Figure 4. NEMO and p62 demonstrate characteristics of phase condensation, with NEMO recruitment dependent on its UBAN domain.

(A) Confocal images of live HeLa cells expressing EGFP-NEMO, Mito-sBFP2, and untagged Parkin, treated with AntA/OligA for 60 min before ("Pre") and after administration of 5% 1,6-Hexanediol.

(B) Confocal image of live HeLa cell expressing EGFP-NEMO, mCherry-p62, Mito-sBFP2, and untagged Parkin, treated with AntA/OligA for 60 min. Box and corresponding insets exhibit the appearance of NEMO and p62-positive mitochondrial puncta (gold arrowhead) before photo-bleaching ("Pre") and its recovery after photo-bleaching. Images were processed to subtract background.

(C) Quantification of fluorescence recovery of EGFP and mCherry after photo-bleaching fluorescent puncta. Data collected from 42 separate photo-bleaching events in 10 cells across 3 independent experiments. (See Figure S4A)

(D) *p62–/–* cells expressing mCherry-Parkin, and EGFP-NEMO were fixed in vehicle or AntA/OligA conditions and labeled with an antibody to HSP60 (Mito) and GFP (488 a-GFP) In zoom images, arrows indicate NEMO recruitment detectable with anti-GFP antibody. Images max-projected 2 μm. (See Figure S4I)

(E) Live HeLa cells expressing EGFP-NEMO^{D304N}, Mito-dsRed2, and untagged Parkin after 50–70 min AntA/OligA treatment. Images max-projected 2 μm. (See Figure S4J)

(F) Average percentages of mitochondria per cell with NEMO recruitment. Data from 3 separate experiments analyzed using Welch's t-test. Error bars indicate SEM; *$P < 0.05$.
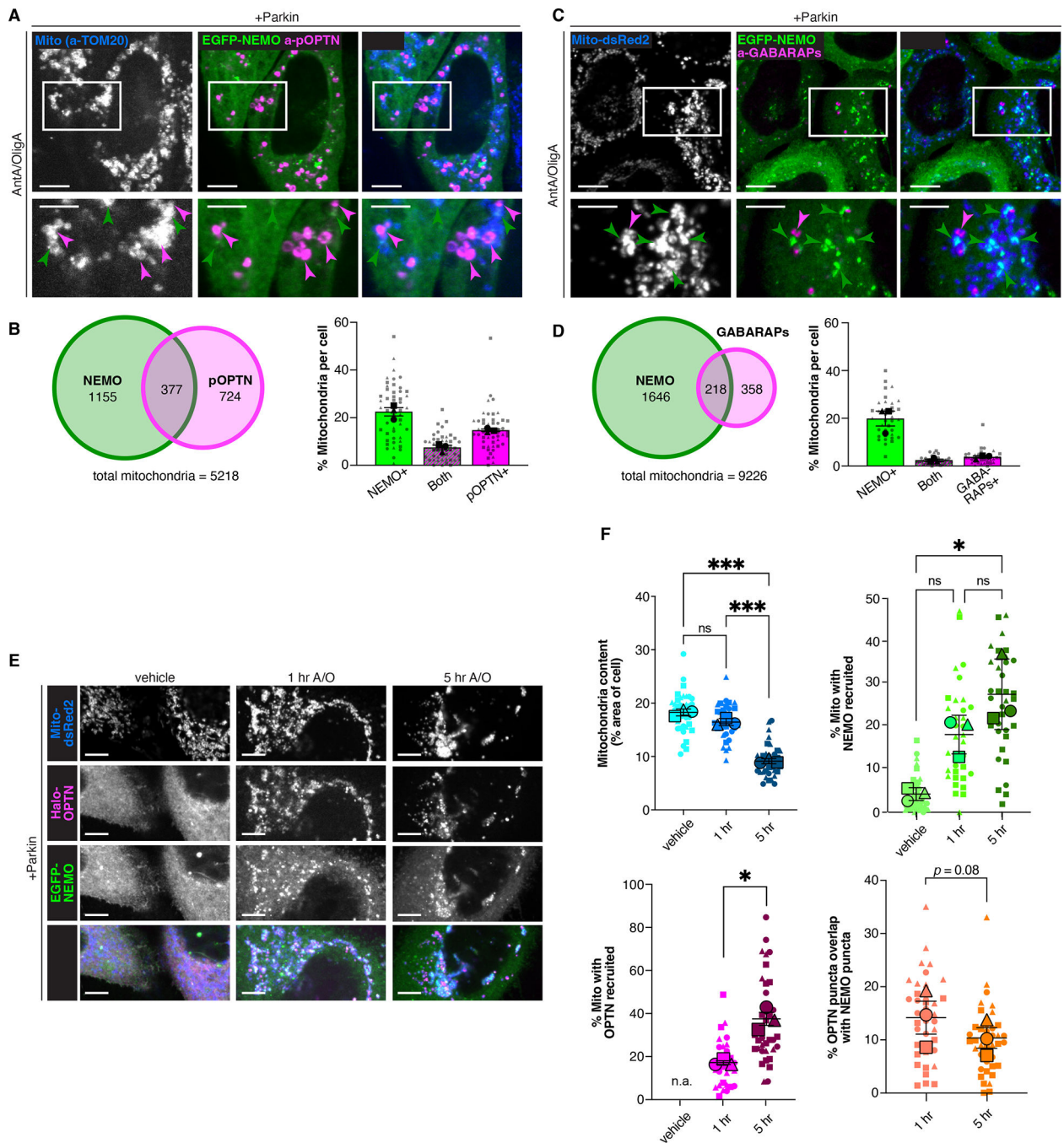
Figure 5. NEMO-positive mitochondria are less likely to become engulfed by autophagosomes.
(A) HeLa cells expressing Mito-dsRed2 (Mito), EGFP-NEMO, and untagged Parkin, were
fixed after AntA/OligA treatment and labeled with an antibody to phosphor-S177-OPTN
(pOPTN). In zoom images (Bottom row), arrows indicate mitochondria with only NEMO
recruitment (green) only pOPTN (magenta) or both (white). Images max-projected 2 μm.
(B) (Left) Euler diagram demonstrating the raw number of mitochondria positive for
NEMO, pOPTN, or both. Remaining mitochondria were positive for neither. (Right)

Average percent of mitochondria per cell positive for only NEMO, only pOPTN, or both. Data collected from 3 independent experiments.

(C) HeLa cells expressing Mito-dsRed2 (Mito), EGFP-NEMO, and untagged Parkin were fixed after AntA/OligA treatment and labeled with an antibody to GABARAPs. In zoom images (Bottom row), arrows indicate mitochondria with only NEMO recruitment (green) only GABARAPs (magenta) or both (white). Images max-projected 2 μm. (See Figure S5A,B)

(D) (Left) Euler diagram demonstrating the raw number of mitochondria positive for NEMO, GABARAPs, or both. The remaining mitochondria were positive for neither. (Right) Average percent of mitochondria per cell positive for only NEMO, only GABARAPs, or both. Data from 3 independent experiments.

(E) HeLa cells expressing Mito-dsRed2, Halo-OPTN, EGFP-NEMO, and untagged Parkin were fixed after treatments as indicated. Images max-projected 2 μm.

(F) Quantification of mitochondrial content proportionate to cell area (Top left) and NEMO (Top right) or OPTN (Bottom left) occupancy on mitochondria in each condition. Data from 3 independent experiments analyzed using one way ANOVA with multiple comparisons (Top) or paired t-tests (Bottom). Error bars indicate SEM; ns, not significant; $*P < 0.05$; $***P$ 0.001. n.a., not applicable.
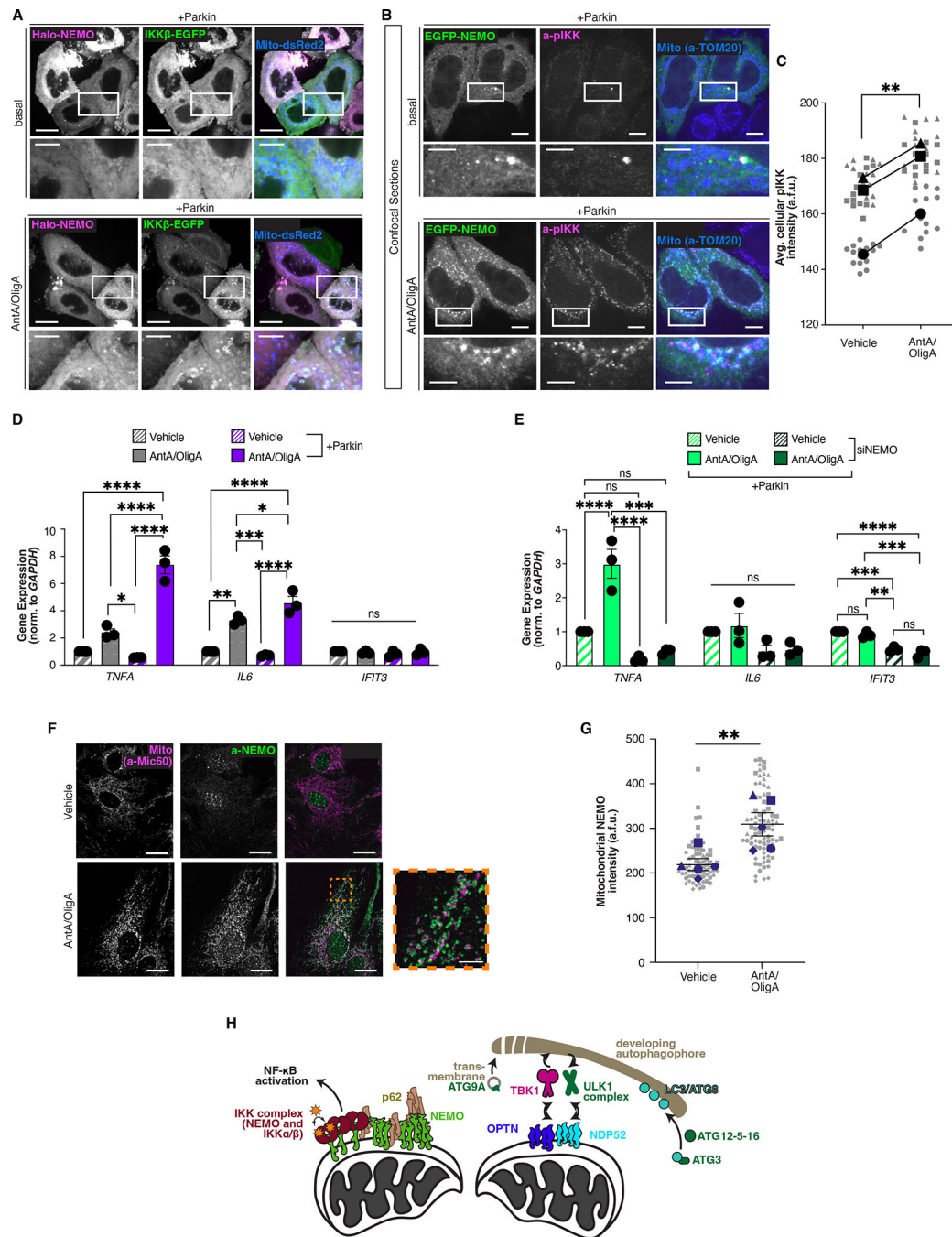
Figure 6. The active IKK complex is recruited to damaged mitochondria in HeLa cells and primary mouse astrocytes.

(A) Live HeLa cells expressing Halo-NEMO, IKKβ-EGFP, Mito-dsRed2 (Mito), and untagged Parkin after 50–70 min AntA/OligA treatment. Images deconvolved and max-projected 2 μm. (See Figure S6A)

(B) Confocal images of a HeLa cell expressing EGFP-NEMO and untagged Parkin, fixed and labeled with antibodies to TOM20 (Mito) and phospho-IKKα/β (pIKK).

(C) Quantification of average pIKK intensity per cell in vehicle or AntA/OligA conditions. Data collected over 3 independent experiments analyzed with a paired t-test. A.f.u., arbitrary fluorescent units; error bars indicate SEM; **P 0.01.

(D) RT-qPCR results for HeLa cells expressing EGFP-NEMO with or without Parkin. Transcripts for *TNFA, IL6,* and *IFIT3* were measured relative to those for *GAPDH*. Data collected from 3 independent experiments analyzed with ordinary one-way ANOVA with multiple comparisons. Error bars indicate SEM; ns, not significant; *$P < 0.05$; **P 0.01; ***P 0.001; ****P 0.0001.

(E) RT-qPCR results for HeLa cells expressing Parkin, with or without siNEMO. Transcripts for *TNFA, IL6,* and *IFIT3* were measured relative to those for *GAPDH*. Data collected from 3 independent experiments analyzed with ordinary one-way ANOVA with multiple comparisons. Error bars indicate SEM; ns, not significant; **P 0.01; ***P 0.001; ****P 0.0001. (See Figure S6B)

(F) Primary murine astrocytes were fixed after 2 hr AntA/OligA treatment and labeled with antibodies to Mic60 (Mito) and NEMO. Images max-projected through the entire cell and displayed with consistent contrast adjustment.

(G) Quantification of mitochondrial NEMO in primary murine astrocytes in vehicle or AntA/OligA conditions. Data collected from 5 independent experiments analyzed with a paired t-test. A.f.u., arbitrary fluorescent units; error bars indicate SEM; **P 0.01.

(H) Model depicting parallel pathways for depolarized mitochondria, with simultaneous induction of autophagosomal clearance via OPTN and Atg8-positive phagophores (Right side of cartoon) and NF-κB activation via a NEMO-mediated signaling platform (Left side).

Key resources table

REAGENT OR RESOURCE	SOURCE	IDENTIFIER
Antibodies		
Mouse monoclonal dsDNA	Millipore	Cat#CBL186; RRID:AB_93367
Rabbit monoclonal GABARAP+GABARAPL1+GABARAPL2	Abcam	Cat#ab109364; RRID:AB_10861928
Mouse monoclonal GAPDH	Abcam	Cat#ab8245; RRID:AB_2107448
Chicken polyclonal GFP for I.F.	Aves	Cat#GFP-1020, RRID:AB_10000240
Mouse monoclonal GFP for W.B.	Abcam	Cat#ab1218, RRID:AB_298911
Rabbit polyclonal HSP60	Sigma-Aldrich	Cat#SAB4501464; RRID:AB_10746162
Mouse monoclonal IKKβ	Novus	Cat#NBP2-33214; RRID:AB_2921267
Rabbit polyclonal LC3B	Abcam	Cat#ab48394; RRID:AB_881433
Rabbit recombinant monoclonal linear Ubiquitin (clone 1E3)	Millipore	Cat#ZRB2114, RRID:AB_2938573
Mouse monoclonal Mitofilin (Mic60)	Abcam	Cat#ab110329, RRID: AB_10859613
Rabbit recombinant NEMO (Figs 6F, S3ES6D)	Abcam	Cat#ab178872; RRID:AB_2847887
Mouse monoclonal NEMO (Figs S1A, S6B)	BDBiosciences	Cat# 611306, RRID:AB_398832
Mouse monoclonal p62	Abcam	Cat#ab56416; RRID:AB_945626
Rabbit monoclonal phospho-IKKα/β (Ser176/180)	Cell Signaling Technology	Cat#2697; RRID:AB_2079382
Rabbit polyclonal phospho-OPTN (Ser177)	Cell Signaling Technology	Cat#57548; RRID:AB_2799529
Rabbit monoclonal phospho-Ubiquitin (Ser65)	Cell Signaling Technology	Cat#62802, RRID:AB_2799632
Mouse monoclonal RBCK1 (HOIL1)	Santa Cruz Biotechnology	Cat#sc-365523, RRID:AB_10841591
Mouse monoclonal TOM20	Santa Cruz Biotechnology	Cat#sc-17764; RRID:AB_628381
Goat anti-Mouse IgG (H+L) Cross-Adsorbed Secondary Antibody, Alexa Fluor 405	Thermo Fisher Scientific	Cat#A31553; RRID:AB_221604
Goat anti-Rabbit IgG (H+L) Cross-Adsorbed Secondary Antibody, Alexa Fluor 405	Thermo Fisher Scientific	Cat#A31556; RRID:AB_221605
Goat anti-Mouse IgG (H+L) Highly Cross-Adsorbed Secondary Antibody, Alexa Fluor 488	Thermo Fisher Scientific	Cat#A11029; RRID:AB_2534088
Goat anti-Rabbit IgG (H+L) Highly Cross-Adsorbed Secondary Antibody, Alexa Fluor 488	Thermo Fisher Scientific	Cat#A11034; RRID:AB_2576217
Goat anti-Chicken IgY (H+L) Secondary Antibody, Alexa Fluor 488	Thermo Fisher Scientific	Cat#A11039; RRID:AB_2534096
Donkey anti-Mouse IgG (H+L) Highly Cross-Adsorbed Secondary Antibody, Alexa Fluor 546	Thermo Fisher Scientific	Cat#A10036; RRID:AB_2534012
Goat anti-Mouse IgG (H+L) Highly Cross-Adsorbed Secondary Antibody, Alexa Fluor Plus 647	Thermo Fisher Scientific	Cat#A32728; RRID:AB_2633277
Donkey anti-Rabbit IgG (H+L) Highly Cross-Adsorbed Secondary Antibody, Alexa Fluor 647	Thermo Fisher Scientific	Cat#A31573; RRID:AB_2536183
IRDye 680RD Donkey anti-Rabbit IgG Secondary Antibody	LI-COR	Cat#926-68073; RRID:AB_10954442
IRDye 800CW Donkey anti-Mouse IgG Secondary Antibody	LI-COR	Cat#926-32212; RRID:AB_621847
Bacterial and virus strains		
pLysS *E. coli* Rosetta (DE3)	Merck	Cat#70956-M
Chemicals and recombinant proteins		

REAGENT OR RESOURCE	SOURCE	IDENTIFIER
Oligomycin A	Millipore Sigma	Cat#75351
Antimycin A	Millipore Sigma	Cat#A8674
Lipofectamine 2000 Transfection Reagent	Thermo Fisher Scientific	Cat#11668019
Lipofectamine RNAiMax Transfection Reagent	Thermo Fisher Scientific	Cat#13778075
Recombinant human TNFα	Peprotech	Cat#300-01A
1,6-Hexanediol	Millipore Sigma	Cat#240117
ChromoTek GFP-Trap Magnetic Particles M-270	Proteintech	Cat#gtd
Janelia Fluor 646 Halo Ligand	Promega	Cat#GA112A
SNAP-Cell 647-SiR	New England Biolabs	Cat#S9102S
Deposited Data		
Original data	this paper	https://doi.org/10.5281/zenodo.8197544
Experimental Models: Cell Lines		
Human: HeLa-M	a gift from A. Peden (Cambridge Institute for Medical Research)	RRID:CVCL_R965
Human: HeLa-OPTN –/–	Lazarou et al, 2015, a gift from R. Youle (NIH)	N/A
Human: HeLa-p62 –/–	Sarraf et al, 2020, a gift from R. Youle (NIH)	N/A
Experimental Models: Organisms/Strains		
Mouse: C57BL6/J	The Jackson Laboratory	strain#000664; RRID:IMSR_JAX:000664
Rat: CD Sprague Dawley IGS	Charles River	strain#001; RRID:RGD_734476
Oligonucleotides		
ON-TARGETplus Human SQSTM1 siRNA	Horizon Discovery	Cat#J-010230-05
ON-TARGETplus Human IKBKG siRNA - SMARTpool	Horizon Discovery	Cat# L-003767-00-0020
ON-TARGETplus Human RBCK1 siRNA	Horizon Discovery	Cat#J-006932-10-0002
ON-TARGETplus Non-targeting siRNA #1	Horizon Discovery	Cat#D-001810-01-20
Primer to *IFIT3* (fwd): TGCAGGGAAACAGCCATCAT	This paper	N/A
Primer to *IFIT3* (rev): GGCATTTCAGCTGTGGAAGG	This paper	N/A
Primer to *IL6* (fwd): AGGAGCCCAGCTATGAACTC	This paper	N/A
Primer to *IL6* (rev): GAGAAGGCAACTGGACCGA	This paper	N/A
Primer to *TNFA* (fwd): GGCCCGACTATCTCGACTTT	This paper	N/A
Primer to *TNFA* (rev): CTCACAGGGCAATGATCCCA	This paper	N/A
Primer to *GAPDH* (fwd): ATCTTCTTTTGCGTCGCCAG	This paper	N/A
Primer to *GAPDH* (rev): GTTGACTCCGACCTTCACCT	This paper	N/A
Recombinant DNA		
Mito-DsRed2	A gift from T. Schwarz (Harvard University)	N/A
Mito-SBFP2	Wong and Holzbaur, 2014	RRID:Addgene_187964
Mito-SNAP	This paper	RRID:Addgene_206480
Parkin	A gift from I. Dikic	RRID:Addgene_187897

REAGENT OR RESOURCE	SOURCE	IDENTIFIER
mCherry-Parkin	Narendra et al., 2008	RRID:Addgene_23956
YFP-Parkin	Narendra et al., 2008	RRID:Addgene_23955
EGFP-mNEMO	Tarantino et al., 2014; a gift from E. Laplantine (Sorbonne Universités)	N/A
EGFP-mNEMO[D304N]	this paper	RRID:Addgene_187898
Halo-mNEMO	this paper	RRID:Addgene_187899
HIS-TEV-mCherry-p62	Wurzer et al., 2015	RRID:Addgene_199780
pGEX-GST-hNEMO	this paper	RRID:Addgene_199781
GST-4XUB	Wurzer et al., 2015	RRID:Addgene_199779
Halo-OPTN	Moore and Holzbaur, 2016	RRID:Addgene_187900
mCherry-vector	Clontech	Cat#632524
mCherry-p62- PB1	Wurzer et al., 2015	RRID:Addgene_187985
mCherry-p62-PB1[AA]	Wurzer et al., 2015	RRID:Addgene_187982
mCherry-p62- UBA	Wurzer et al., 2015	RRID:Addgene_187984
mCherry-p62-LIR[AAAA]	Wurzer et al., 2015	RRID:Addgene_187981
mCherry-p62-TIR[AAA]	this paper	RRID:Addgene_187901
IKKβ/IKK2-EGFP	Birbach et al., 2002	RRID:Addgene_111195
Halo-NDP52	Promega	Cat#FHC03487
EGFP-Ubiquitin	this paper	RRID:Addgene_187910
Software and Algorithms		
Volocity v6.3.1	PerkinElmer	https://www.volocity4d.com/; RRID:SCR_002668
Visiview v5.0.0.24	Visitron System	https://www.visitron.de/products/visiviewr-software.html; RRID:SCR_022546
Leica Application Suite X v3.0.3.16319	Leica Microsystems,	https://www.leica-microsystems.com/products/microscope-software/p/leica-las-x-ls/; RRID:SCR_013673
ZEN v2.3	Zeiss	https://www.zeiss.com/microscopy/us/home.html; RRID:SCR_013672
Illustrator v25.2.1	Adobe	http://www.adobe.com/products/illustrator; RRID:SCR_010279
QuantStudio Design and Analysis v1.4.1	ThermoFisher,	https://www.thermofisher.com/us/en/home/global/forms/life-science/quantstudio-3-5-software; RRID:SCR_020238
Huygen's Professional v17.10	Scientific Volume Imaging,	https://svi.nl/Huygens-Software; RRID:SCR_014237
Ilastik v1.3.0	Berg et al, 2019	http://ilastik.org/; RRID:SCR_015246
FIJI/ImageJ v2.3.0/1.53f	Schindelin et al, 2012,	https://imagej.net/; RRID:SCR_003070
Image Studio v5	LI-COR	https://www.licor.com/bio/image-studio/; RRID:SCR_015795
GraphPad v9	Prism	http://www.graphpad.com/; RRID:SCR_002798

REAGENT OR RESOURCE	SOURCE	IDENTIFIER
RStudio v1.0.143	Posit	http://www.rstudio.com/; RRID:SCR_000432
Other		
Protocol: Astrocyte isolation and culturing	Schildge, et al., 2013	dx.doi.org/10.17504/protocols.io.e6nvwdp9wlmk/v1
Protocol: Expression and purification of human p62 (HIS-TEV-mCherry-p62)	Wurzer et al., 2015	dx.doi.org/10.17504/protocols.io.j8nlkob61v5r/v1
Protocol: Expression and purification of human NEMO (GST-GFP-NEMO)	This paper	dx.doi.org/10.17504/protocols.io.261gedpojv47/v1
Protocol: Microscopy-based bead protein-protein interaction assay	This paper	dx.doi.org/10.17504/protocols.io.dm6gp3erpvzp/v1
Protocol: Live imaging and analysis to investigate phase separation properties of NEMO during mitophagy	This paper	dx.doi.org/10.17504/protocols.io.j8nlkw7rxl5r/v1
Protocol: Fixing hippo neurons to assess endogenous NEMO during oxidative stress	This paper	dx.doi.org/10.17504/protocols.io.e6nvwjx8dlmk/v1
Protocol: Image processing to investigate NEMO recruitment and involvement in mitophagy and inflammatory signaling	This paper	dx.doi.org/10.17504/protocols.io.n2bvj61xxlk5/v1
Protocol: Cell lysis and gel electrophoresis for protein analysis of HeLa cells	This paper	dx.doi.org/10.17504/protocols.io.j8nlkk1w1l5r/v1
Protocol: HeLa culture, transfection, and labeling of Halo-fusion proteins	This paper	dx.doi.org/10.17504/protocols.io.yxmvmnb66g3p/v1
Protocol: Live imaging to investigate mitophagy kinetics and NEMO recruitment in HeLa-M cells	This paper	dx.doi.org/10.17504/protocols.io.rm7vzy9w5lx1/v1
Protocol: Fixation and imaging of HeLa cells after mitochondrial depolarization	This paper	dx.doi.org/10.17504/protocols.io.n92ldz6oxv5b/v1
Protocol: RNA extraction and quantitative PCR to assay inflammatory gene expression	This paper	dx.doi.org/10.17504/protocols.io.5qpvob15bl4o/v1